

---

**Supplementary information**

---

**Atomically dispersed antimony on carbon nitride for the artificial photosynthesis of hydrogen peroxide**

---

In the format provided by the  
authors and unedited

**Atomically Dispersed Antimony on Carbon Nitride for the Artificial Photosynthesis of Hydrogen Peroxide**

Zhenyuan Teng,<sup>1,7,8</sup> Qitao Zhang,<sup>2,8</sup> Hongbin Yang,<sup>3,8</sup> Kosaku Kato,<sup>4</sup> Wenjuan Yang,<sup>2</sup> Ying-Rui Lu,<sup>5</sup> Sixiao Liu,<sup>6,7</sup> Chengyin Wang,<sup>6,7</sup> Akira Yamakata,<sup>4</sup> Chenliang Su,<sup>2,\*</sup> Bin Liu,<sup>3,\*</sup> and Teruhisa Ohno<sup>1,7,\*</sup>

<sup>1</sup>Department of Applied Chemistry, Faculty of Engineering, Kyushu Institute of Technology, Kitakyushu 804-8550, Japan

<sup>2</sup>International Collaborative Laboratory of 2D Materials for Optoelectronics Science and Technology of Ministry of Education, Institute of Microscale Optoelectronics, Shenzhen University, Shenzhen 518060, China

<sup>3</sup>School of Chemical and Biomedical Engineering, Nanyang Technological University, 62 Nanyang Drive, Singapore 637459, Singapore

<sup>4</sup>Graduate School of Engineering, Toyota Technological Institute, 2-12-1 Hisakata, Tempaku Nagoya 468-8511, Japan

<sup>5</sup>National Synchrotron Radiation Research Center, Hsinchu 30076, Taiwan

<sup>6</sup>College of Chemistry and Chemical Engineering, Yangzhou University, 180 Si-Wang-Ting Road, Yangzhou 225002, China

<sup>7</sup>Joint Laboratory of Yangzhou University, Kyushu Institute of Technology, Yangzhou University, 180 Si-Wang-Ting Road, Yangzhou 225002, China

<sup>8</sup>These authors contributed equally.

ORCID:

Teruhisa Ohno: <https://orcid.org/0000-0002-7825-8189>

Chenliang Su: <https://orcid.org/0000-0002-8453-1938>

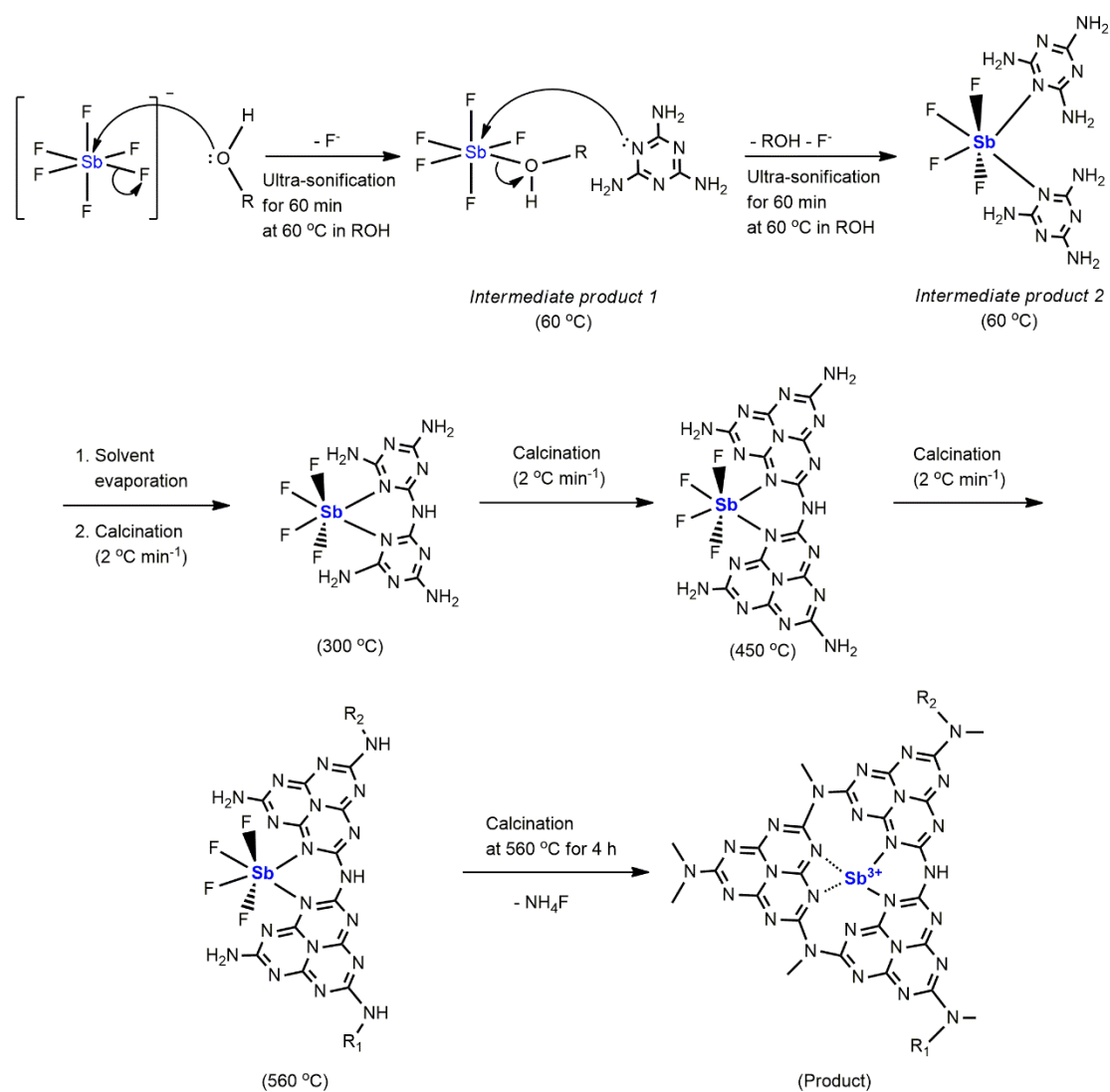
Bin Liu: <https://orcid.org/0000-0002-4685-2052>

E-mail address:

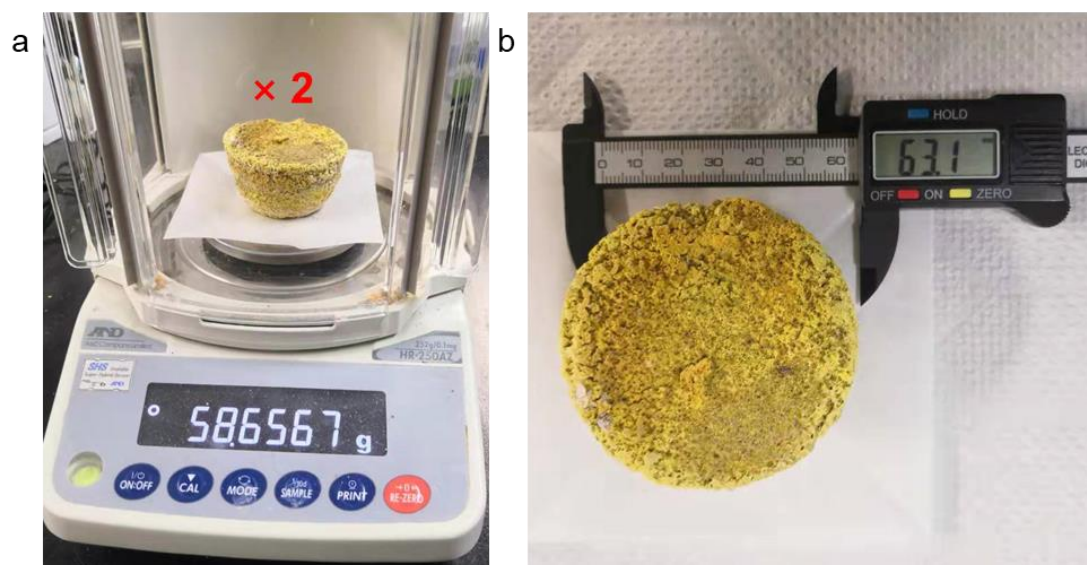
Teruhisa Ohno: [tohno@che.kyutech.ac.jp](mailto:tohno@che.kyutech.ac.jp)

Chenliang Su: [chmsuc@nus.edu.sg](mailto:chmsuc@nus.edu.sg)

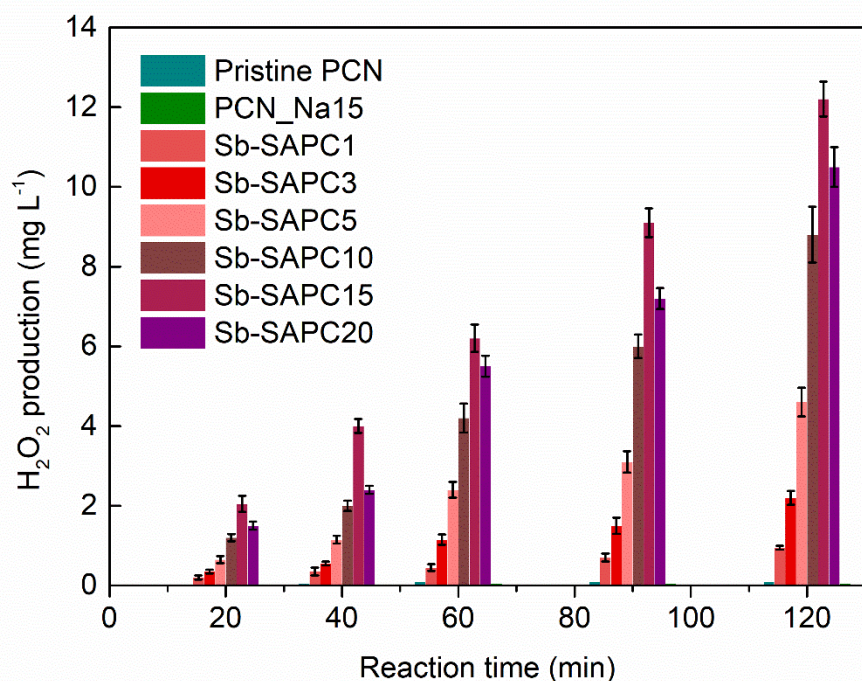
Bin Liu: [liubin@ntu.edu.sg](mailto:liubin@ntu.edu.sg)



**Supplementary Figure 1. The preparation procedure of the single Sb atom photocatalyst (Sb-SAPC).** Dashed bonds in the product refers to the weak interaction between N and Sb atoms.

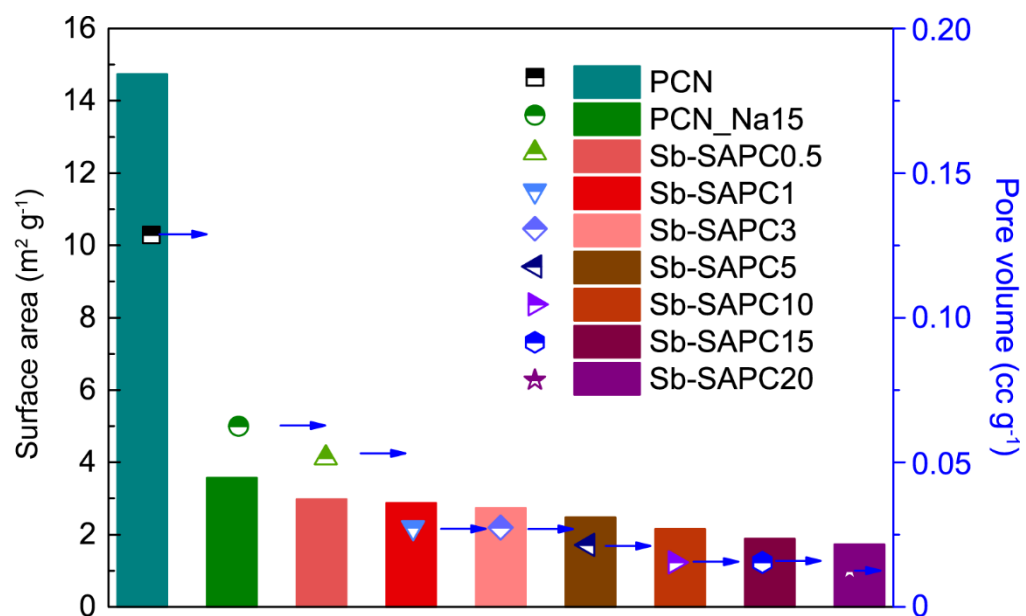


**Supplementary Figure 2 | Digital photographs showing the as-prepared Sb-SAPC15 in one batch.**

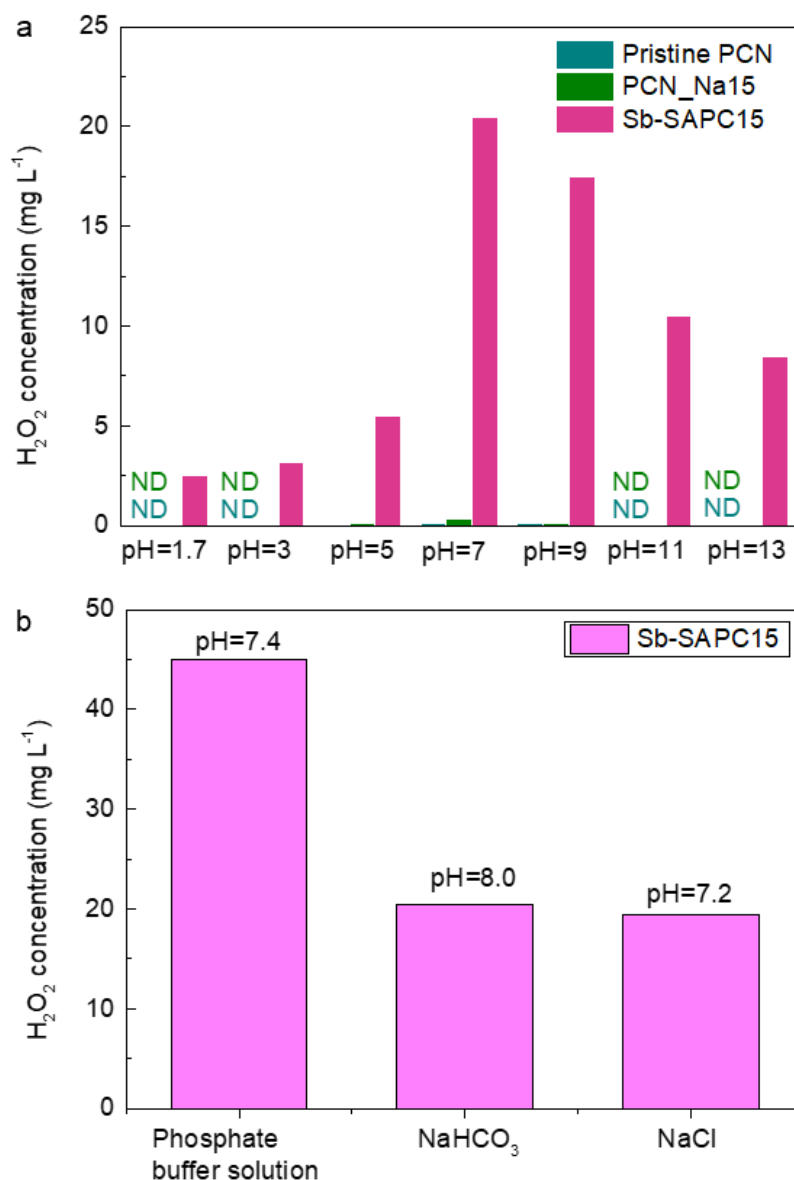


**Supplementary Figure 3 | Comparison of activities of Sb-SAPCs and PCNs for photocatalytic  $\text{H}_2\text{O}_2$  production** (light source: Xe lamp, light intensity at 420–500 nm:  $30.3 \text{ W m}^{-2}$ ; reaction medium: water at pH = 10.1 for Sb-SAPC15). Error bars represent the standard deviations of 3 replicate measurements.

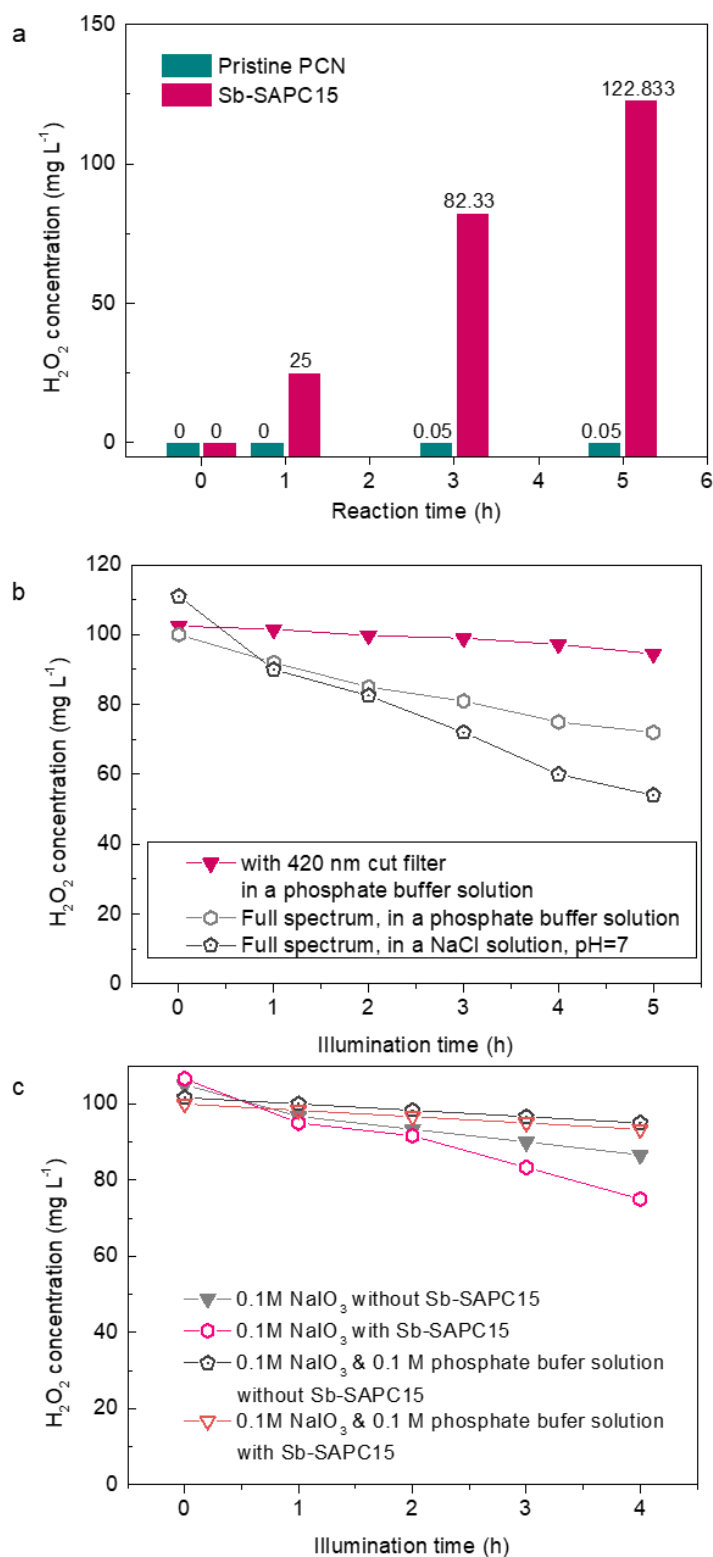
The pH of the Sb-SAPC15 aqueous suspension (solvent is pure water) is 10.1 because addition of Sb-SAPC15 particles significantly accelerated self-ionization of water. The zeta potential of Sb-SAPC15 reached -30 mV in an acid solution, indicating that Sb-SAPC15 could be recognized as a solid-state Lewis base. Addition of Lewis base into pure water could accelerate water self-ionization, thus leading to a significantly increased pH.



**Supplementary Figure 4 | Specific surface area and average pore volume of PCN, PCN\_Na15 and Sb-SAPCx.**



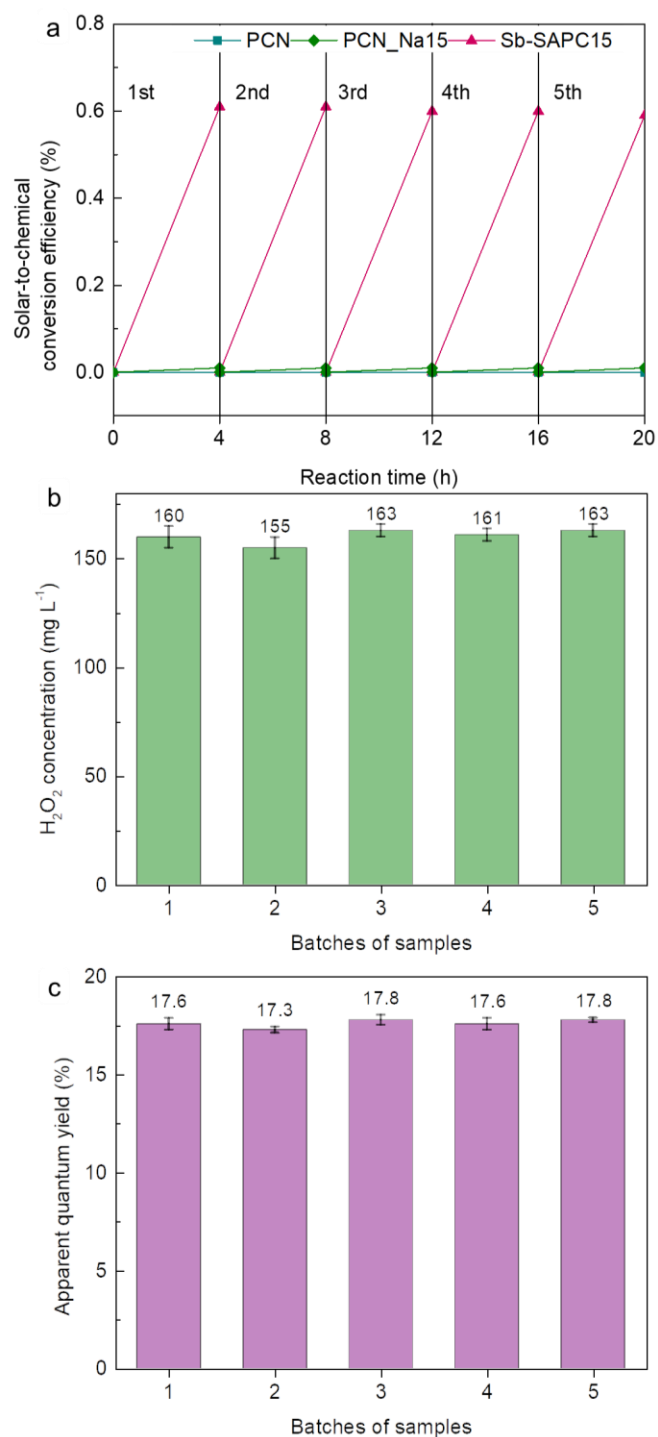
**Supplementary Figure 5 | Optimization experiments for non-sacrificial photocatalytic H<sub>2</sub>O<sub>2</sub> production. a, pH optimization. b, Solvent optimization. (light source: Xe lamp, light intensity at 420–500 nm: 30.3 W m<sup>-2</sup>). The reaction time is 90 min.**



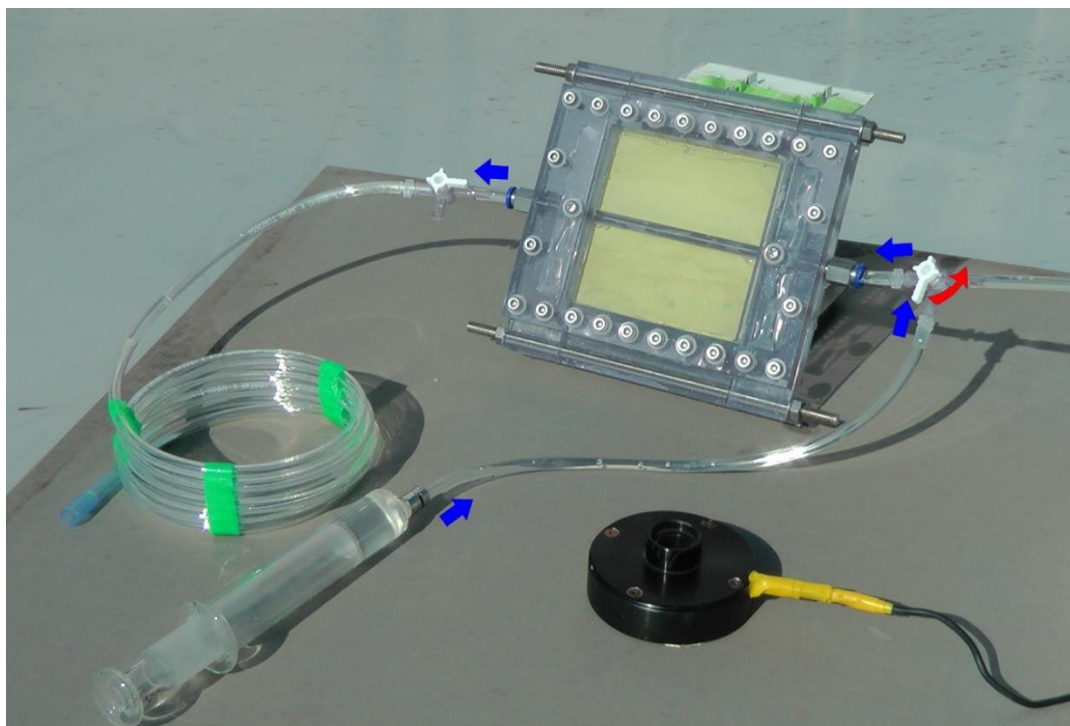
**Supplementary Figure 6 | Long term activity for non-sacrificial photocatalytic H<sub>2</sub>O<sub>2</sub> production.** **a**, Long term photocatalytic H<sub>2</sub>O<sub>2</sub> production using Sb-SAPC15 and pristine PCN as the photocatalyst. **b**, Optimization for light wavelength for H<sub>2</sub>O<sub>2</sub> degradation study. **c**, Interactions between photogenerated holes and H<sub>2</sub>O<sub>2</sub> in different kinds of solutions. The solution was irradiated by a 300 W Xenon Lamp with a UV cut filter (light intensity: 30.3 W m<sup>-2</sup> at 420-500 nm).



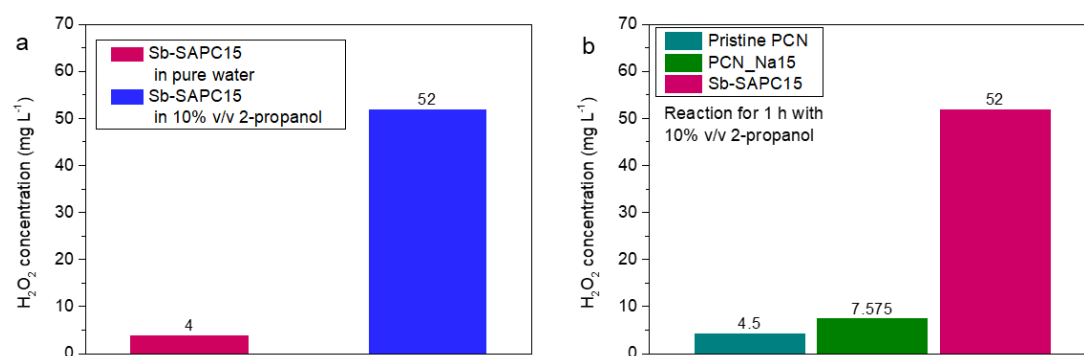
The change in concentration of  $\text{H}_2\text{O}_2$  with an electron acceptor versus time was plotted to investigate whether the holes transferred to  $\text{H}_2\text{O}_2$  ([Supplementary Figure 6c](#)). The concentration of  $\text{H}_2\text{O}_2$  gradually decreased in 0.1 M  $\text{NaIO}_3$  without Sb-SAPC since slight decomposition of  $\text{H}_2\text{O}_2$  was unavoidable under visible light irradiation with high light intensity. After addition of Sb-SAPC15, the decomposition of  $\text{H}_2\text{O}_2$  was accelerated, indicating that the transfer of photogenerated holes could decompose  $\text{H}_2\text{O}_2$  in 0.1 M  $\text{NaIO}_3$  solution. This phenomenon further confirmed that  $\text{H}_2\text{O}_2$  could serve as a hole scavenger, which should be considered during the photocatalytic  $\text{H}_2\text{O}_2$  production. However, addition of the phosphate buffer solution could significantly suppress the decomposition of  $\text{H}_2\text{O}_2$ . These results indicate the crucial role of phosphate buffer solution, which is able to stabilize the produced  $\text{H}_2\text{O}_2$  during the photocatalytic process.



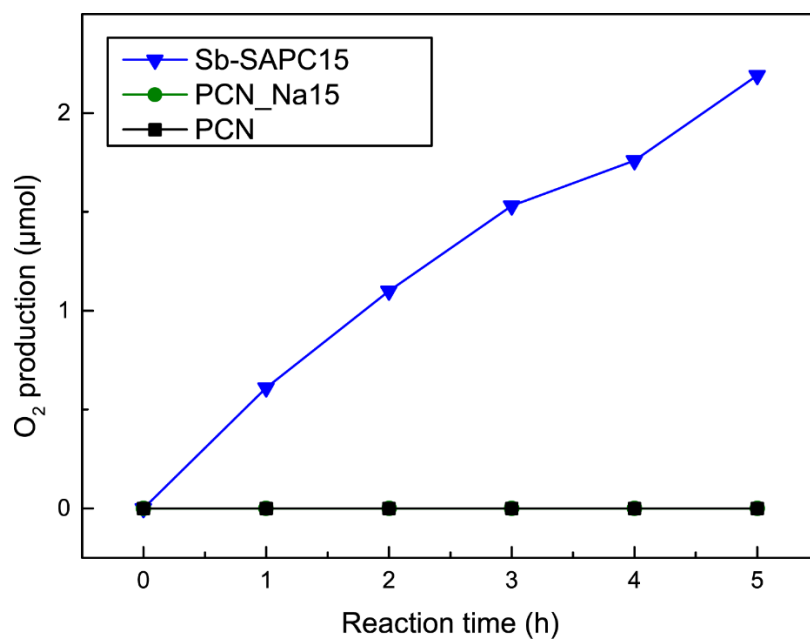
**Supplementary Figure 7 | Repeatability and reproducibility of catalysts.** **a**, Repeatability of the CN samples for photocatalytic production of H<sub>2</sub>O<sub>2</sub>. After each run, the catalyst was filtered and re-suspended in a fresh solution with pH adjusted to 7.4 by phosphate buffer solution. **b**, Reproducibility of photocatalytic H<sub>2</sub>O<sub>2</sub> production for calculating solar-to-chemical conversion efficiency. **c**, Reproducibility for apparent quantum yield ( $\lambda = 420$  nm). Light source: Xe lamp, light intensity at 420–500 nm: 30.3 W m<sup>-2</sup>; reaction medium: phosphate buffer solution at pH = 7.4. Error bars represent the standard deviation of 3 replicate measurements.



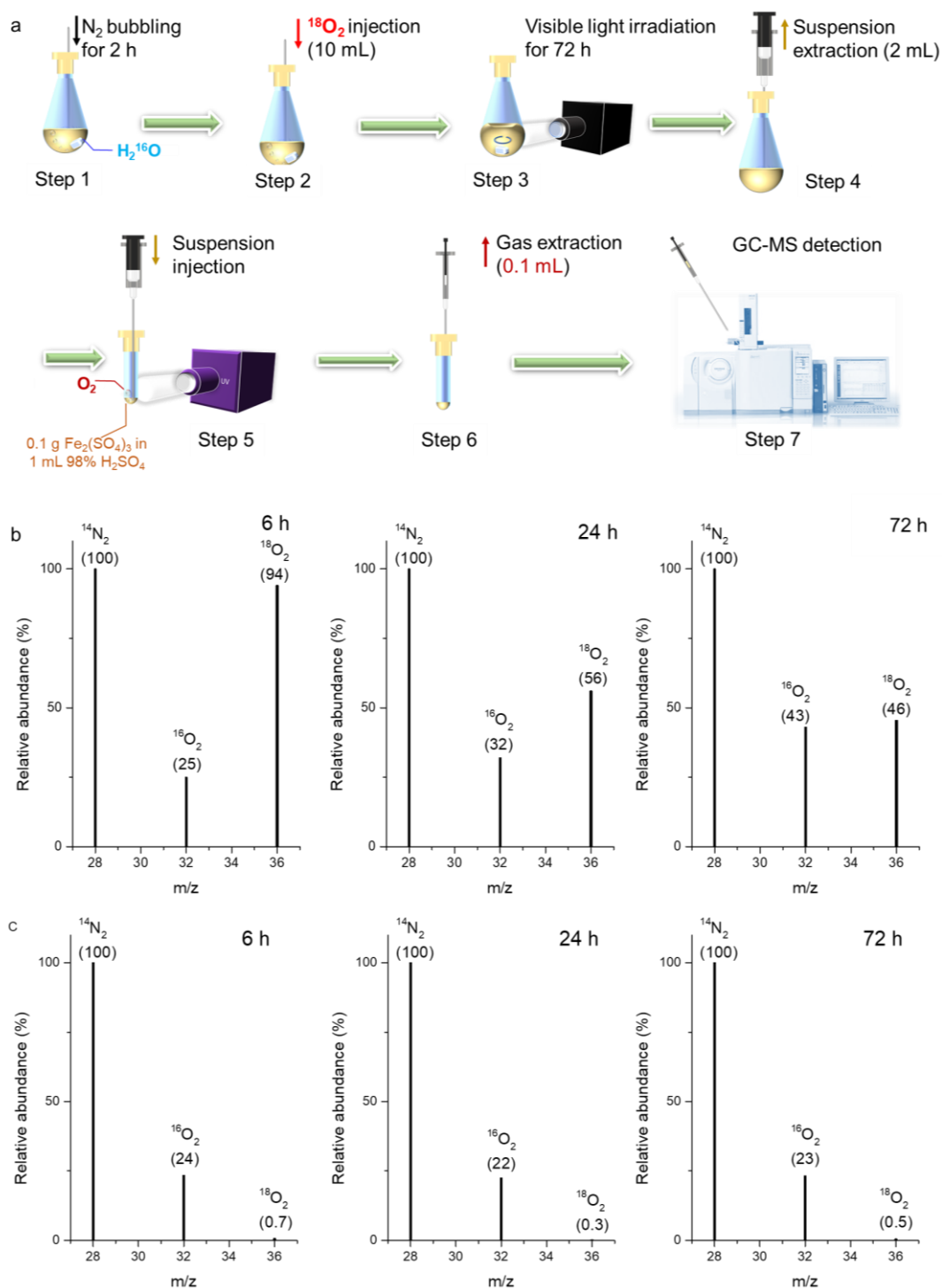
**Supplementary Figure 8 | The practical experiment of photocatalytic H<sub>2</sub>O<sub>2</sub> production using solar light.** The blue arrow indicates the flow direction of aqueous solution. The red arrow tells the direction to open the valve.



**Supplementary Figure 9 | Half reaction with addition of an electron donor. a,** Comparison of H<sub>2</sub>O<sub>2</sub> formed in pure water and 10% (v/v) 2-propanol aqueous solution catalyzed by Sb-SAPC15. **b,** Comparison of H<sub>2</sub>O<sub>2</sub> production in 10% (v/v) 2-propanol aqueous solution catalyzed by pristine PCN, PCN\_Na15 and Sb-SAPC15. Reaction time: 60 min. Irradiation condition:  $\lambda > 420$  nm (Xe lamp, light intensity at 400–500 nm: 30.3 W m<sup>-2</sup>), at 298 K.

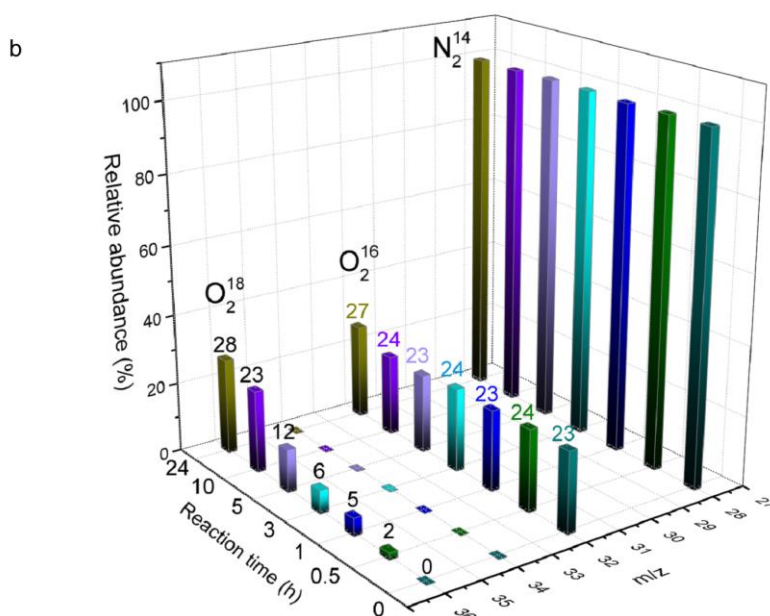
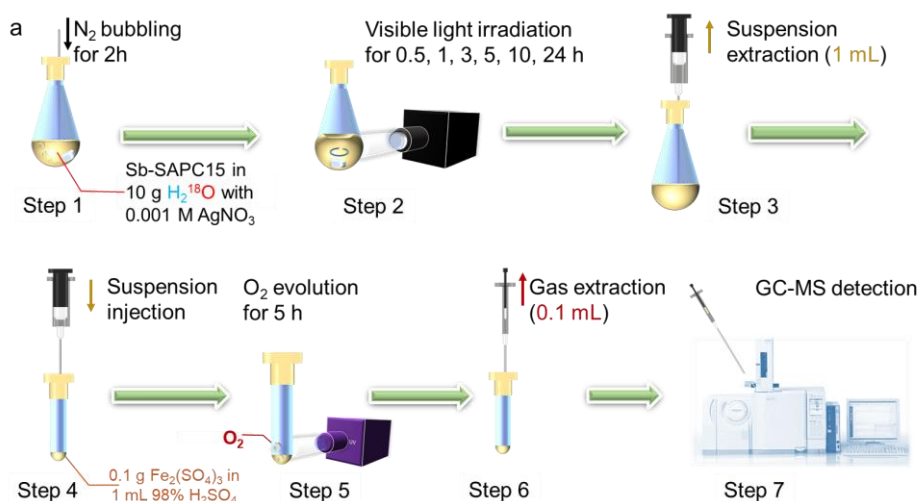


**Supplementary Figure 10 | Comparison of oxygen evolution efficiency for PCN, PCN\_Na15 and Sb-SAPC15 during the half reaction.**



**Supplementary Figure 11 | Isotopic experiments utilizing  $^{18}\text{O}_2$ .** **a**, Schematic diagram showing the isotopic experimental procedure for  $\text{H}_2\text{O}_2$  production with addition of  $^{18}\text{O}_2$  as the electron acceptor (The figure of GC-MS in step 7 is taken from <https://www.an.shimadzu.co.jp/gcms/2010se.htm>). **b**, GC-MS spectra of the gas extracted from the Sb-SAPC15/ $\text{Fe}^{3+}$  system after the light illumination for 6 h, 24 h and 72 h in step 3. **c**, GC-MS spectra of the gas extracted from the same system without addition of Sb-SAPC15 at the reaction time point of 6 h, 24 h and 72 h in step 3. The reaction solution is pure  $\text{H}_2^{16}\text{O}$  with injection of 10 mL  $^{18}\text{O}_2$ .

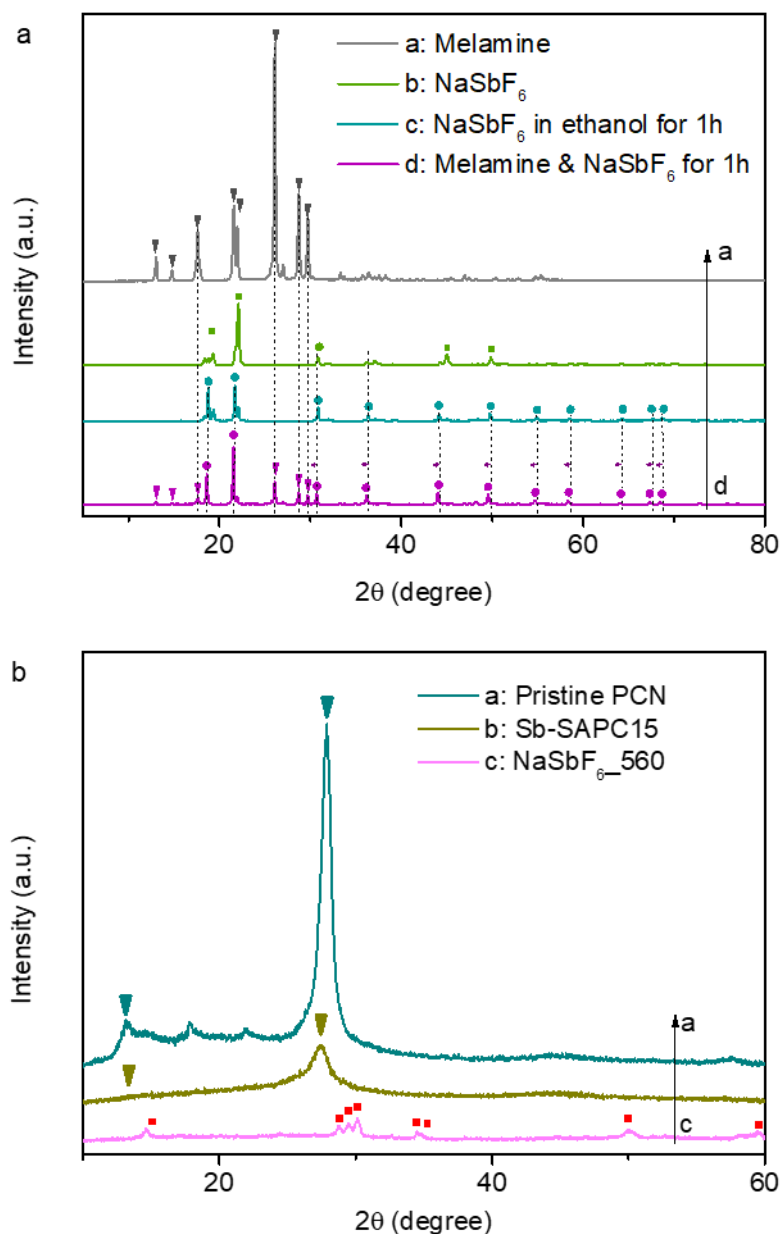
We have performed control experiment to ensure that the  $^{18}\text{O}_2$  injected at the beginning of the experiment could be barely measured later. The details for the experiment are as follows: all experiments are the same as the experimental procedure except the addition of the photocatalyst. In this case, the  $\text{H}_2\text{O}_2$  could hardly be formed, and only dissolved oxygen existed in the liquid phase<sup>1</sup>. As shown in step 3, the dissolved oxygen could be transferred to step 4 when liquid was extracted from the solution. The gas extracted from step 6 was also measured by GC-MS. As shown in the figure above, we could hardly detect the signal of  $^{18}\text{O}_2$ , indicating that the dissolved oxygen in the extracted solution (step 3) barely influenced the measurement. Note that the signal of  $^{16}\text{O}_2$  is attributed to the small leakage of  $\text{O}_2$  during the injection process.



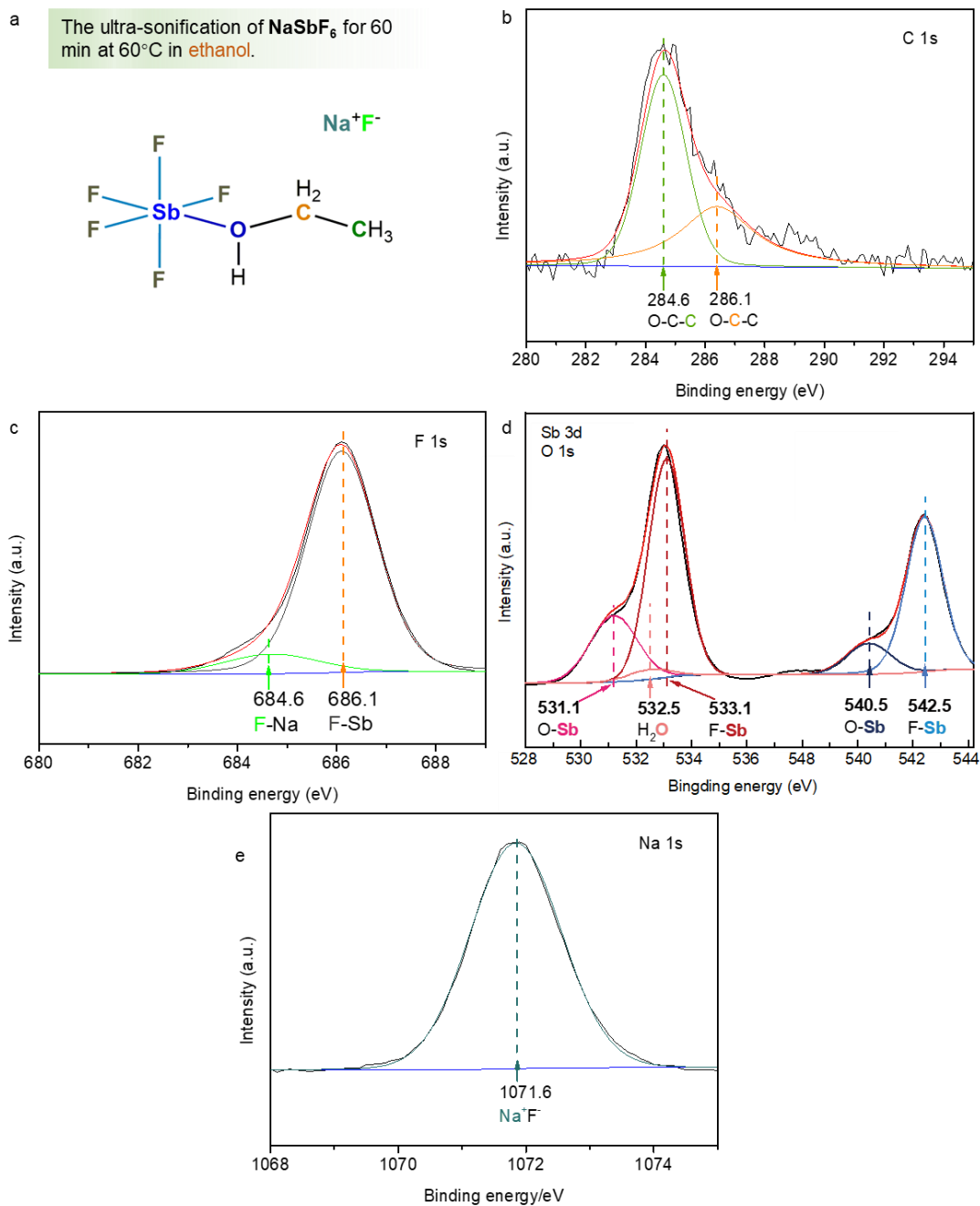
**Supplementary Figure 12 | Isotopic experiments utilizing  $\text{H}_2^{18}\text{O}$ .** **a**, Schematic diagram showing the isotopic experimental procedure for  $\text{H}_2\text{O}_2$  production with addition of  $\text{Ag}^+$  as the electron acceptor (The figure of GC-MS in step 7 is taken from <https://www.an.shimadzu.co.jp/gcms/2010se.htm>). **b**, GC-MS spectra of the gas extracted from the Sb-SAPC15/ $\text{Fe}^{3+}$  system after the Xenon lamp illumination of 0 h, 0.5 h, 1 h, 3 h, 5 h, 10 h and 24 h in step 2. The reaction solution is pure  $\text{H}_2^{18}\text{O}$  with saturated ultrapure  $\text{N}_2$ . (Mass of the catalyst in step 1: 50 mg,  $\text{Ag}^+$  concentration: 0.001M).

The signal of  $^{16}\text{O}_2$  is attributed to the small leakage of  $\text{O}_2$  during the injection process (step 7) since the signals of  $^{16}\text{O}_2$  are almost the same (~23 %). Similar phenomenon could be also observed in the Supplementary Figure 11c even no  $^{16}\text{O}_2$  was injected in the system. Although this system error existed, the increasing signal of  $^{18}\text{O}_2$  with extended reaction time still revealed the water oxidation gradually happened with the addition of the electron acceptor.

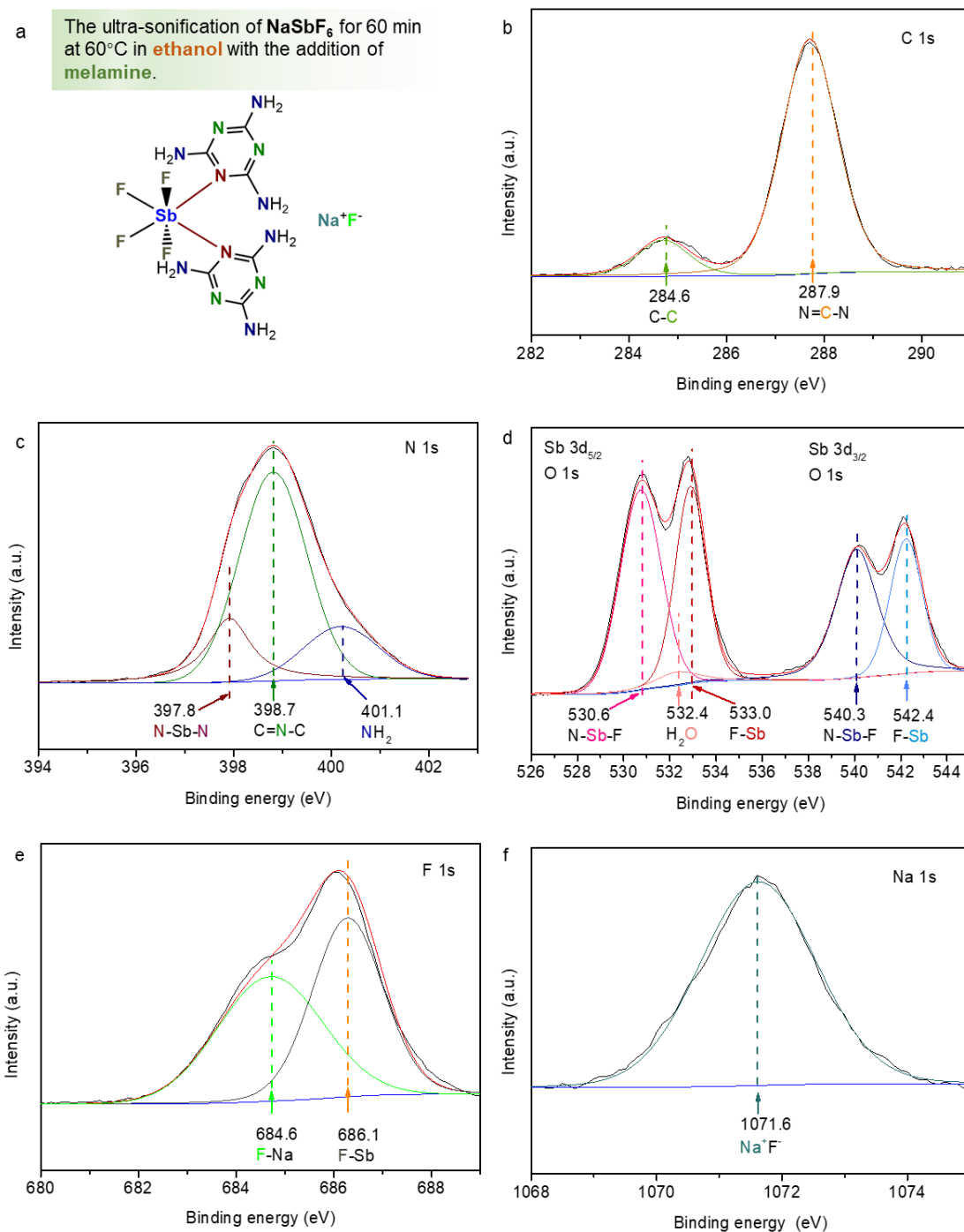




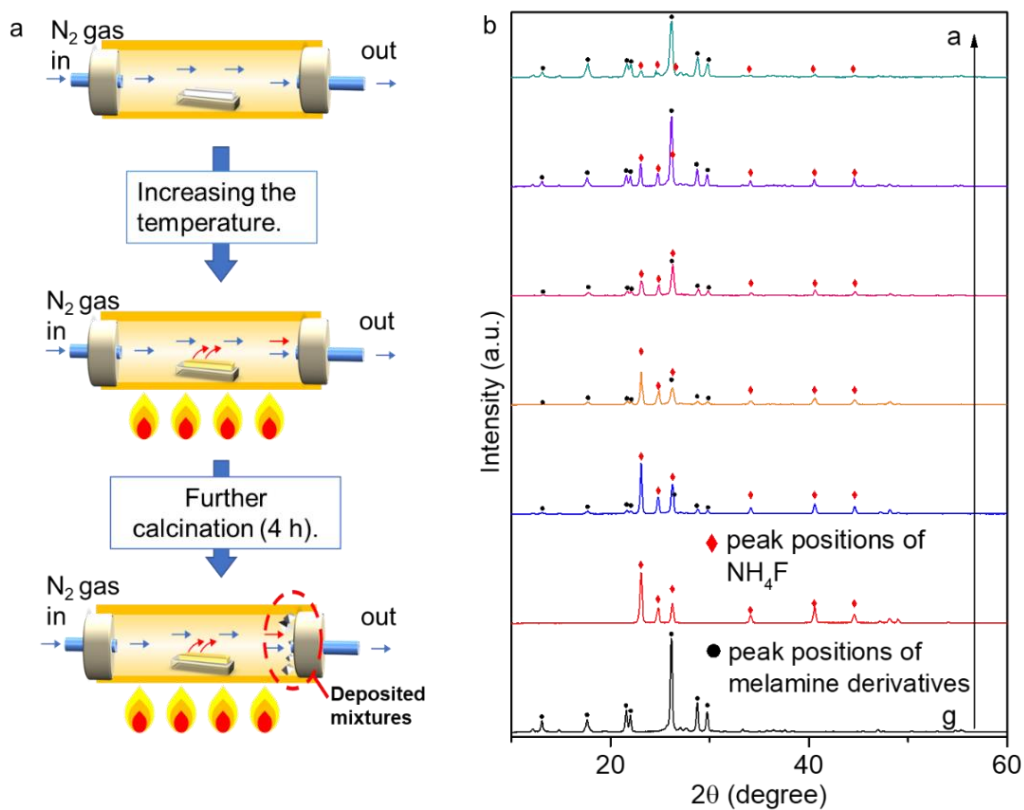
**Supplementary Figure 13 | X-ray diffraction (XRD) patterns.** **a**, XRD patterns of melamine (patten a),  $\text{NaSbF}_6$  (patten b), c: 3.881 g  $\text{NaSbF}_6$  in ethanol with sonification for 1 hour (*Intermediate Product 1* in *Supplementary Figure 1*, patten c) and sample c mixed with 4 g of melamine in ethanol with 1 hour sonification (*Intermediate Product 2* in *Supplementary Figure 1*, patten d). **b**, XRD patterns of pristine PCN, Sb-SAPC15 and  $\text{NaSbF}_6$  prepared at 560 °C for 4 h ( $\text{NaSbF}_6_{560}$ ).



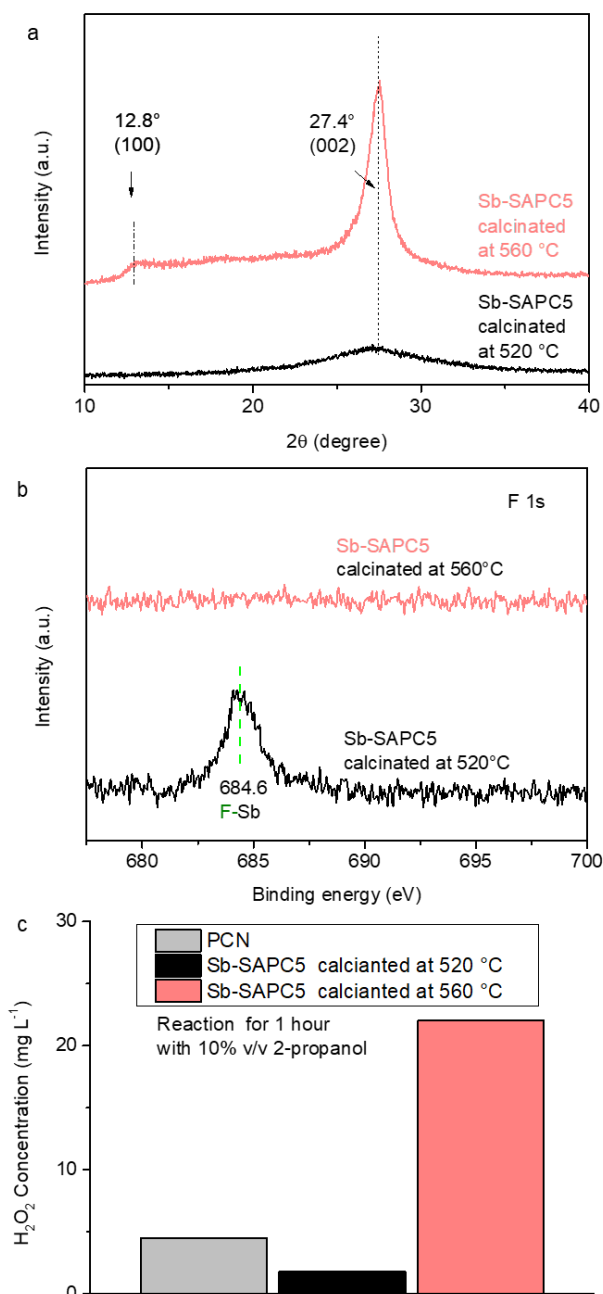
**Supplementary Figure 14 | XPS spectra of 3.881 g  $\text{NaSbF}_6$  in ethanol with sonification for 1 hour (Intermediate Product 1 in Supplementary Figure 1). a, Structure of Intermediate Product 1. b-e, High-resolution XPS spectra of C 1s (b), F 1s (c), Sb3d & O 1s (d) and Na 1s (e).**



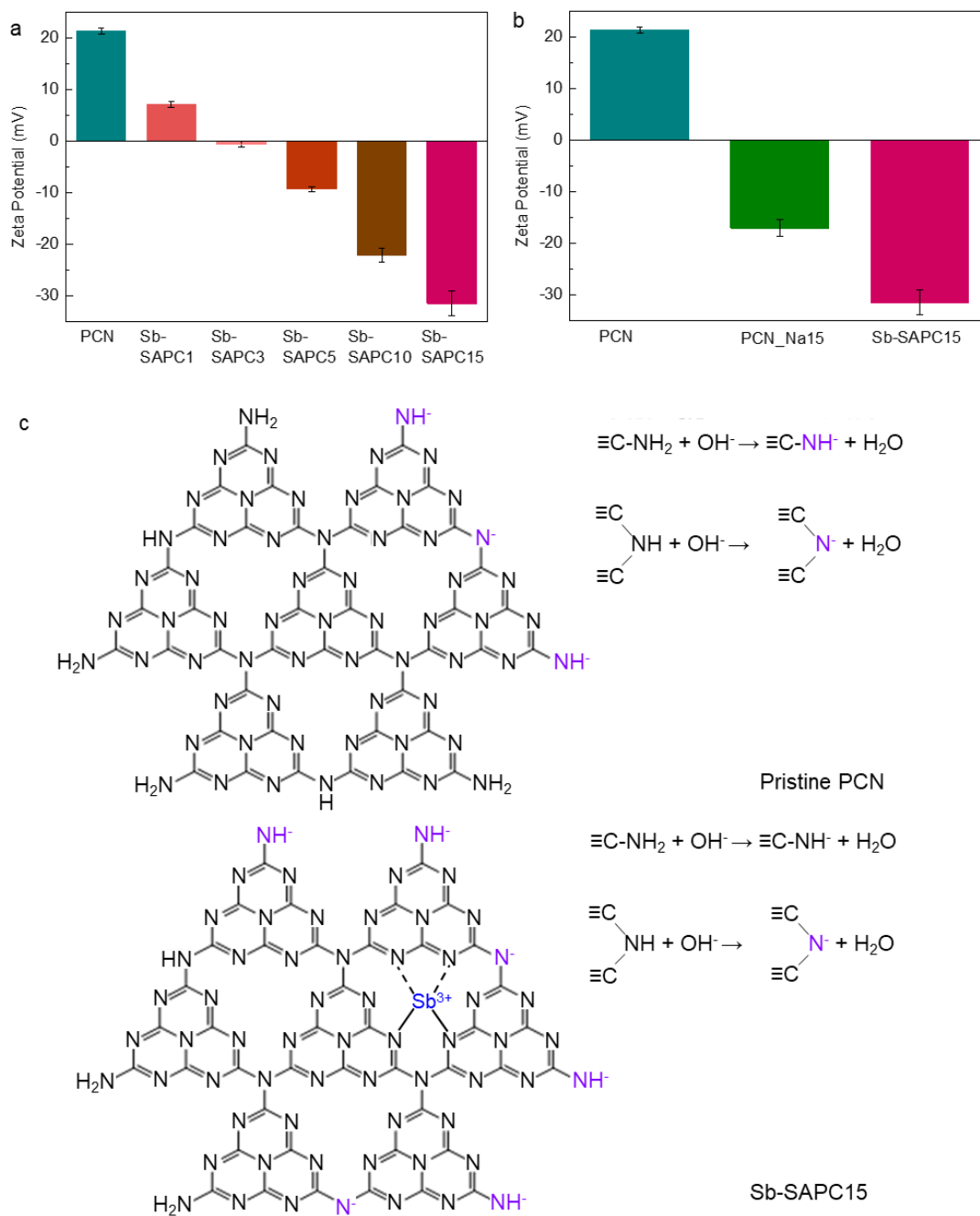
**Supplementary Figure 15 | XPS spectra of 3.881 g  $\text{NaSbF}_6$  in ethanol with sonification for 1 hour, followed by mixed with 4 g of melamine in ethanol with 1 hour sonification (*Intermediate Product 2* in *Supplementary Figure 1*). a, Structure of *Intermediate Product 2*. b-f, High-resolution XPS spectra of C 1s (b), N 1s (c), Sb3d & O 1s (d), F 1s (e) and Na 1s (f).**



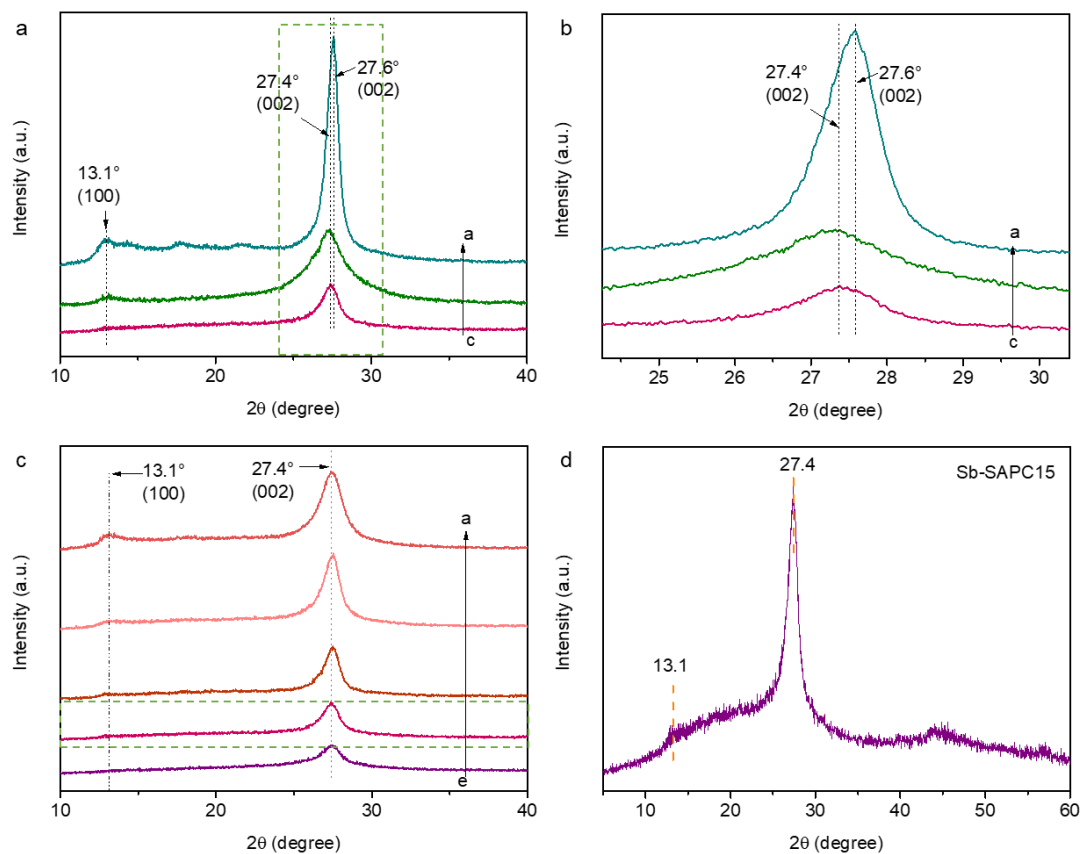
**Supplementary Figure 16 | Characterization of the deposited mixture on the silicone plug of the tube furnace.** **a**, A schematic diagram showing the deposition process during calcination. **b**, XRD patterns of the deposited mixture obtained during preparation of Sb-SAPC1 (pattern a), Sb-SAPC3 (pattern b), Sb-SAPC5 (pattern c), Sb-SAPC10 (pattern d), and Sb-SAPC15 (pattern e). XRD patterns of pure NH<sub>4</sub>F (pattern f) and the deposited mixture during preparation of PCN (pattern g) are also included as references.



**Supplementary Figure 17 | Comparison of Sb-SAPCs prepared at different temperatures.** **a-b** XRD patterns (**a**) and high-resolution F 1s spectra (**b**) of Sb-SAPC5 prepared at 520 °C and 560 °C. **c**, Comparison of H<sub>2</sub>O<sub>2</sub> formed 10% (v/v) 2-propanol aqueous solution catalyzed by PCN and Sb-SAPC5 prepared at 520 °C and 560 °C. Reaction time: 60 min. Irradiation condition:  $\lambda > 420$  nm (Xe lamp, light intensity at 400–500 nm: 30.3 W m<sup>-2</sup>), at 298 K.

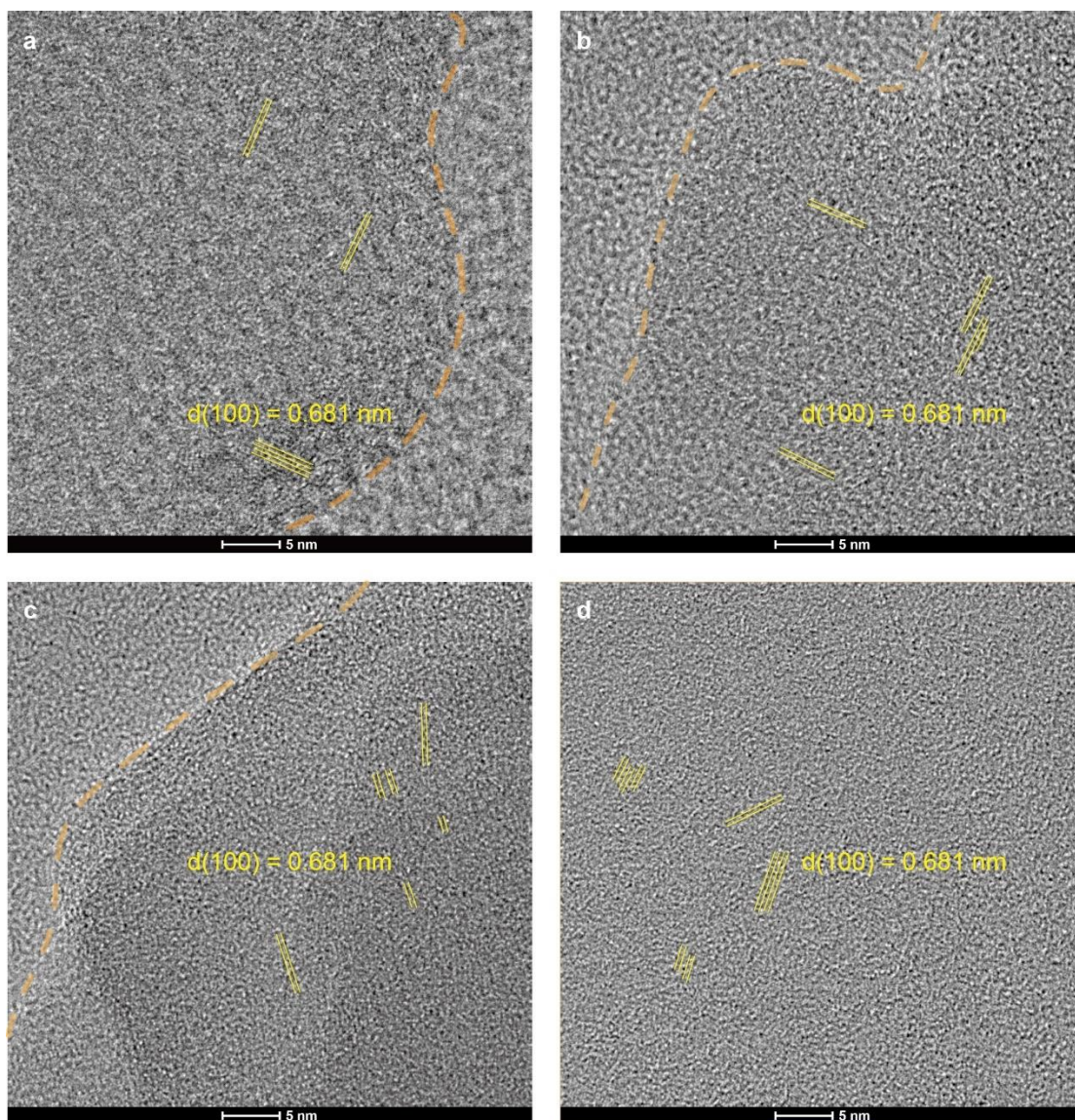


**Supplementary Figure 18 | Surface charge of Sb-SAPCs and PCN samples at pH = 3.**  
**a**, Zeta-potential of Sb-SAPCs with different Sb contents. **b**, Zeta-potential of PCN, PCN\_Na15 and Sb-SAPC15. **c**, The possible mechanism of gradually increased surface negativity of Sb-SAPCs.



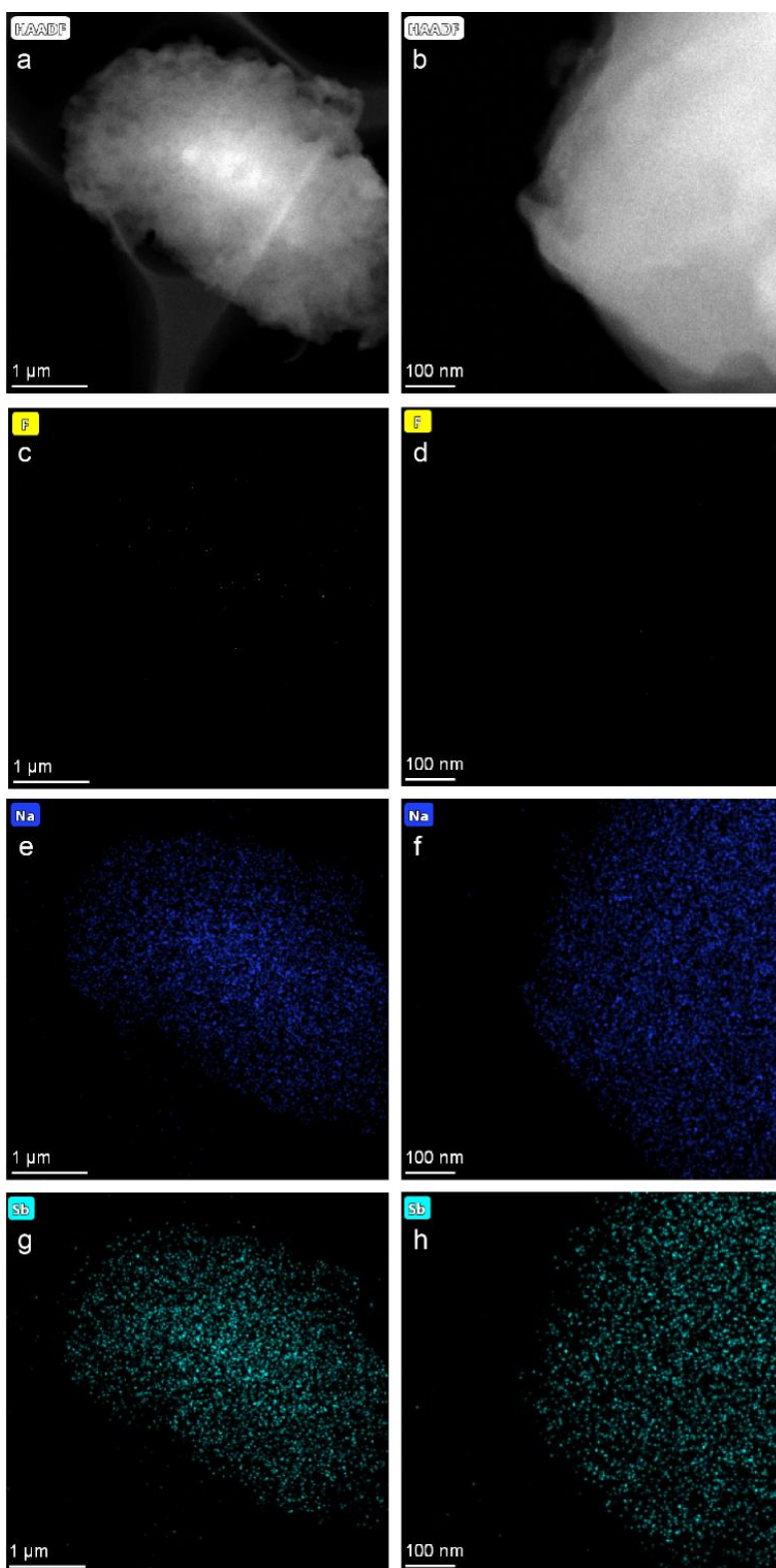
**Supplementary Figure 19 | Crystallinity characterized by X-ray diffraction.** **a**, XRD patterns of a: pristine PCN; b: PCN\_Na15; and c: Sb-SAPC15. **b**, XRD patterns (high-resolution) of carbon nitride samples. **c**, XRD patterns of a: Sb-SAPC1; b: Sb-SAPC5; c: Sb-SAPC10; d: Sb-SAPC15; and e: Sb-SAPC20. **d**, XRD patterns (high-resolution) of Sb-SAPC15.



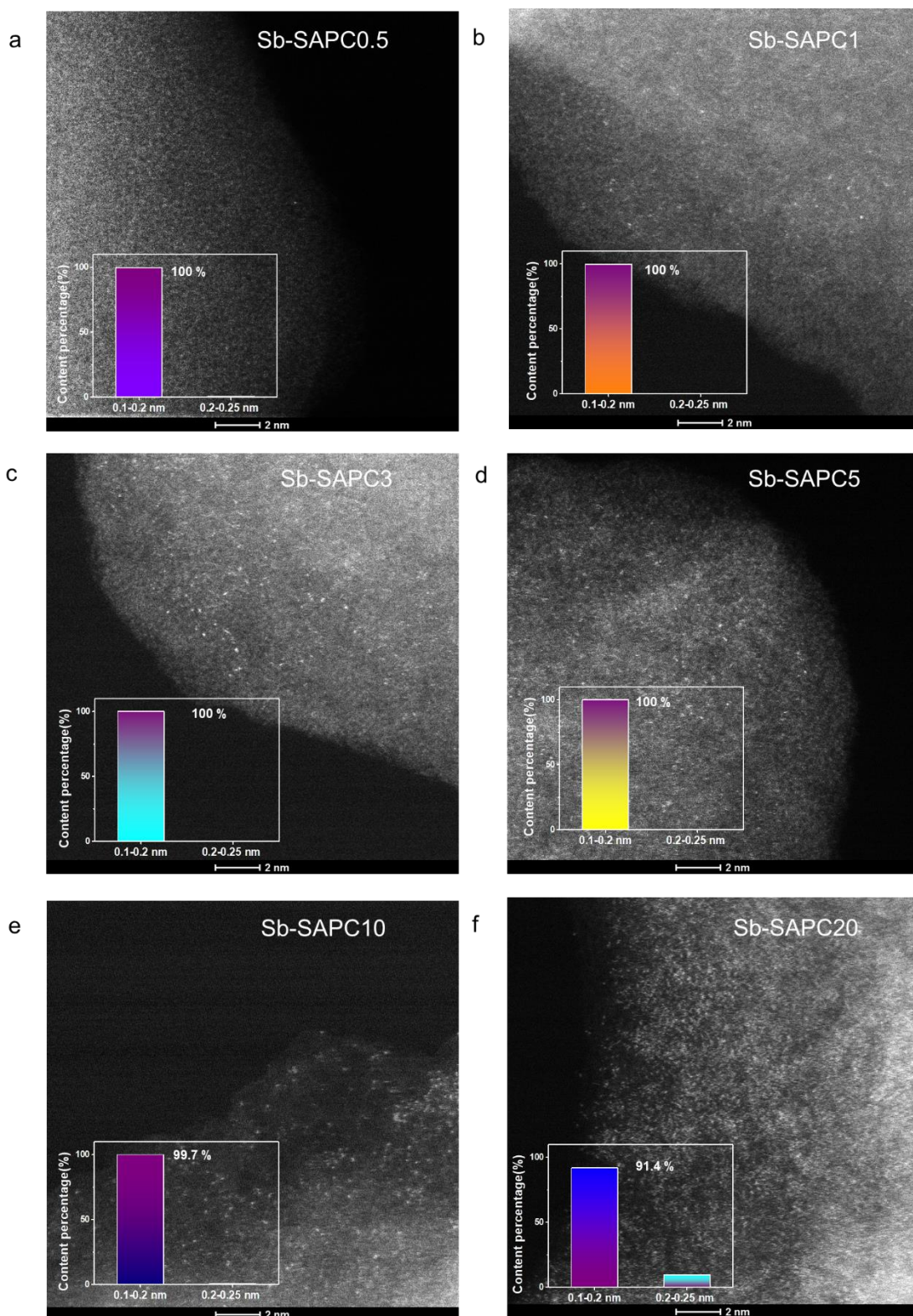


**Supplementary Figure 20 | Crystallinity characterized by high-resolution transmission electron microscopy. a-d, HR-TEM images of Sb-SAPC1 (a), Sb-SAPC5 (b), Sb-SAPC10 (c) and Sb-SAPC15 (d). The yellow line indicates the lattice fringe of the (100) plane of PCN.**

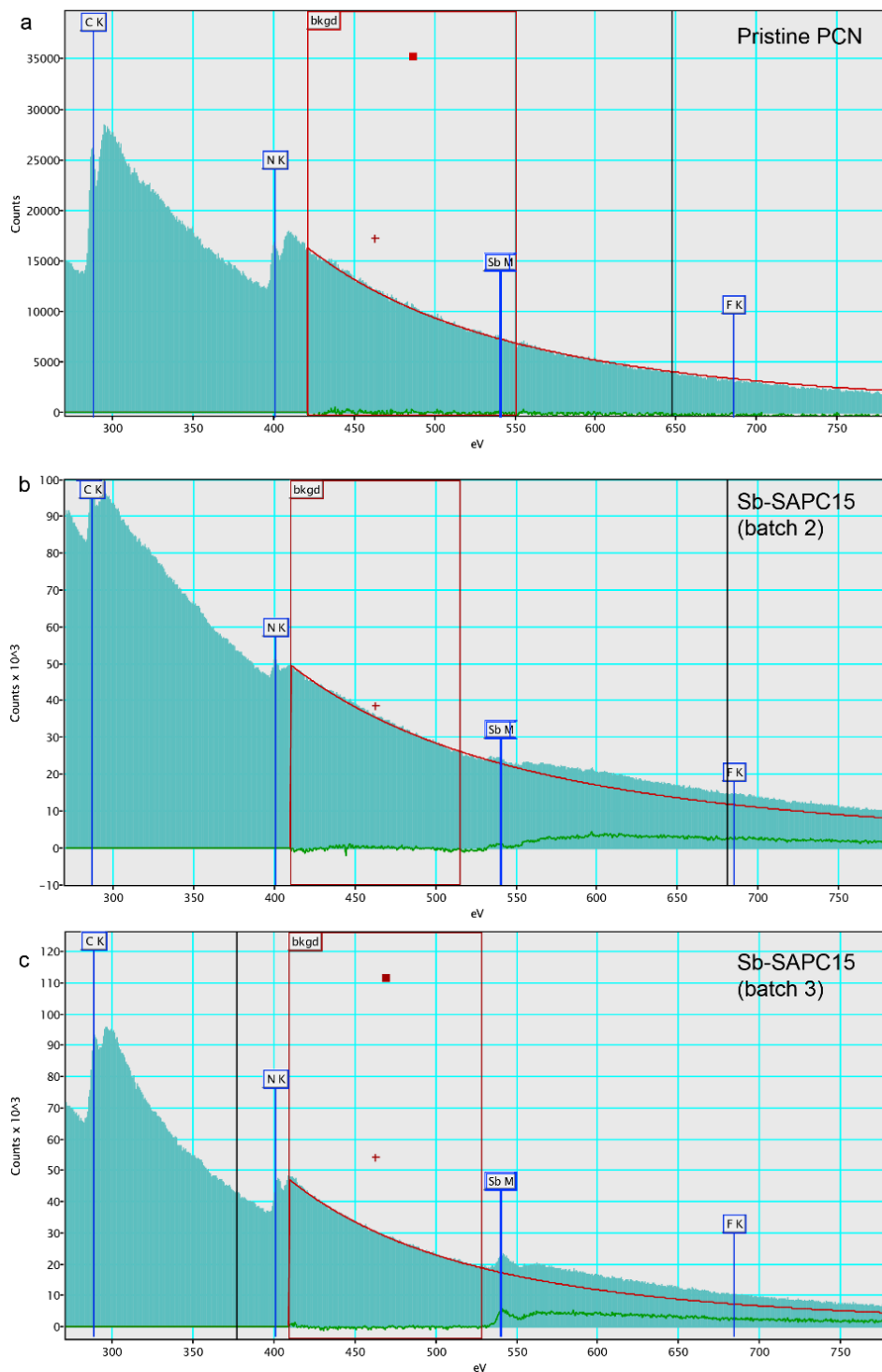




**Supplementary Figure 21 | Elemental distribution in Sb-SAPC15.** **a-b**, Low and high-magnification HAADF-STEM images of Sb-SAPC15. **c-h**, The corresponding EDS elemental mapping images of F (**c-d**), Na (**e-f**) and Sb (**g-h**) at low and high-magnification.

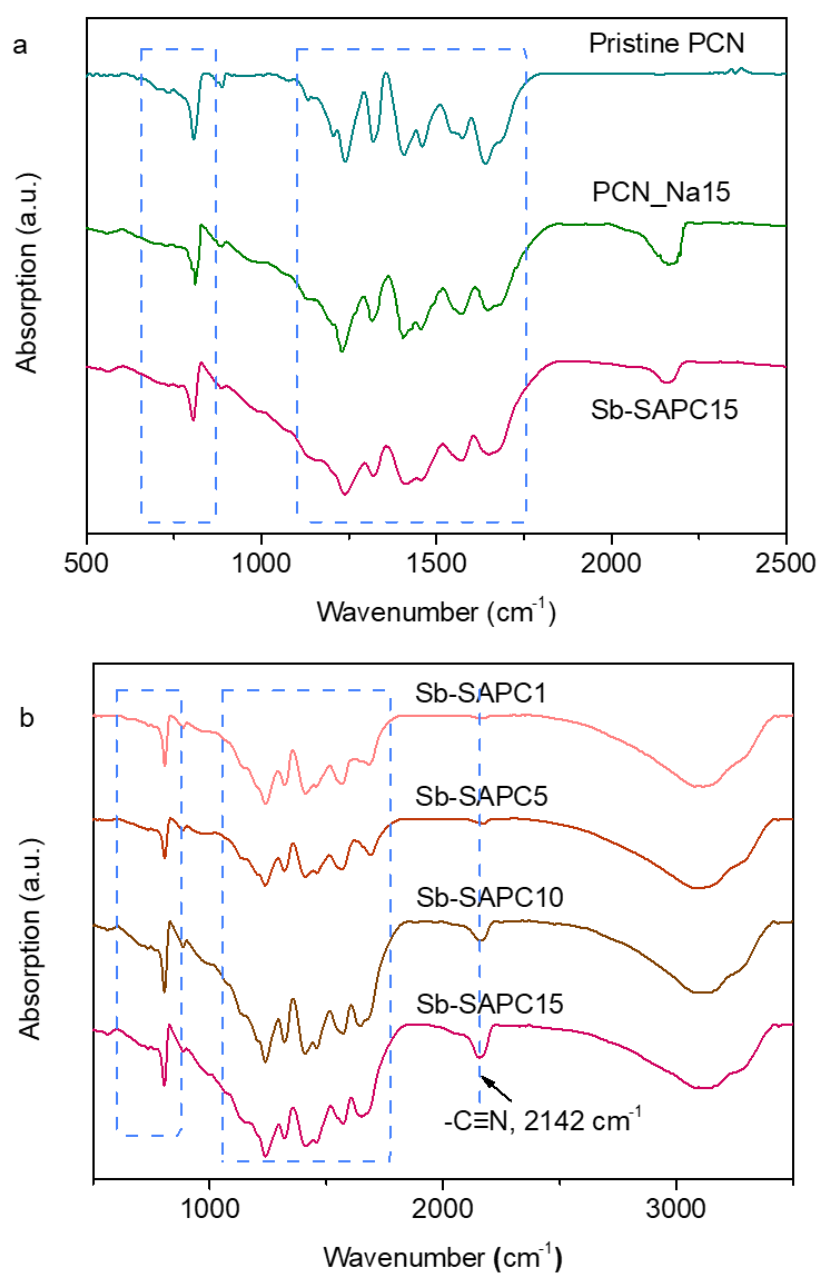


**Supplementary Figure 22 | Characterization of isolated Sb species in Sb-SAPCs with different Sb contents. a-f**, HAADF-STEM images of Sb-SAPC0.5 (a), Sb-SAPC1 (b), Sb-SAPC3 (c), Sb-SAPC5 (d), Sb-SAPC10 (e) and Sb-SAPC20 (f). Inset shows the size distribution of the bright spots.

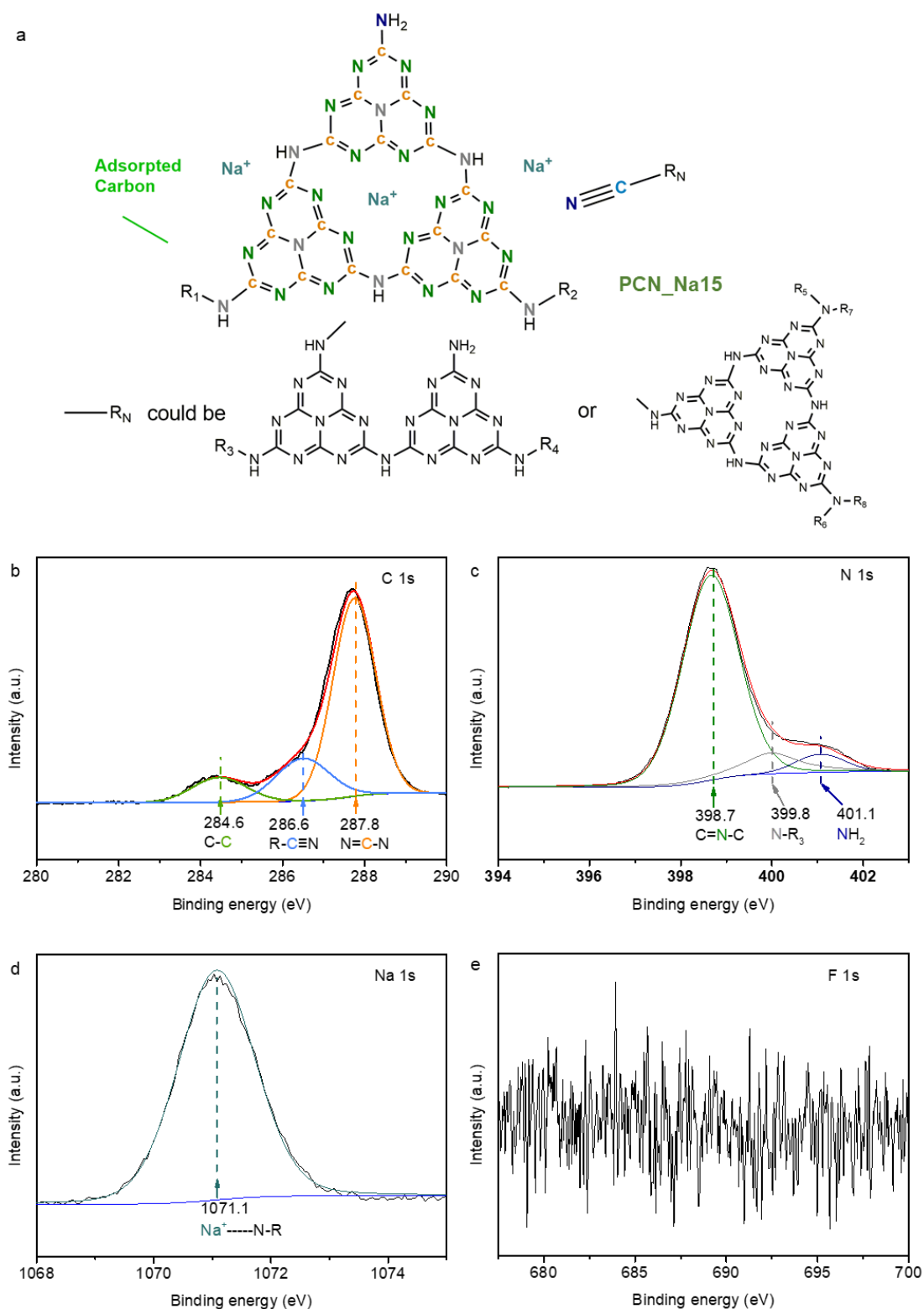


**Supplementary Figure 23 | EELS spectra of CN samples. a, pristine PCN. b, Sb-SAPC15 (batch 2). c, Sb-SAPC15 (batch 3).**

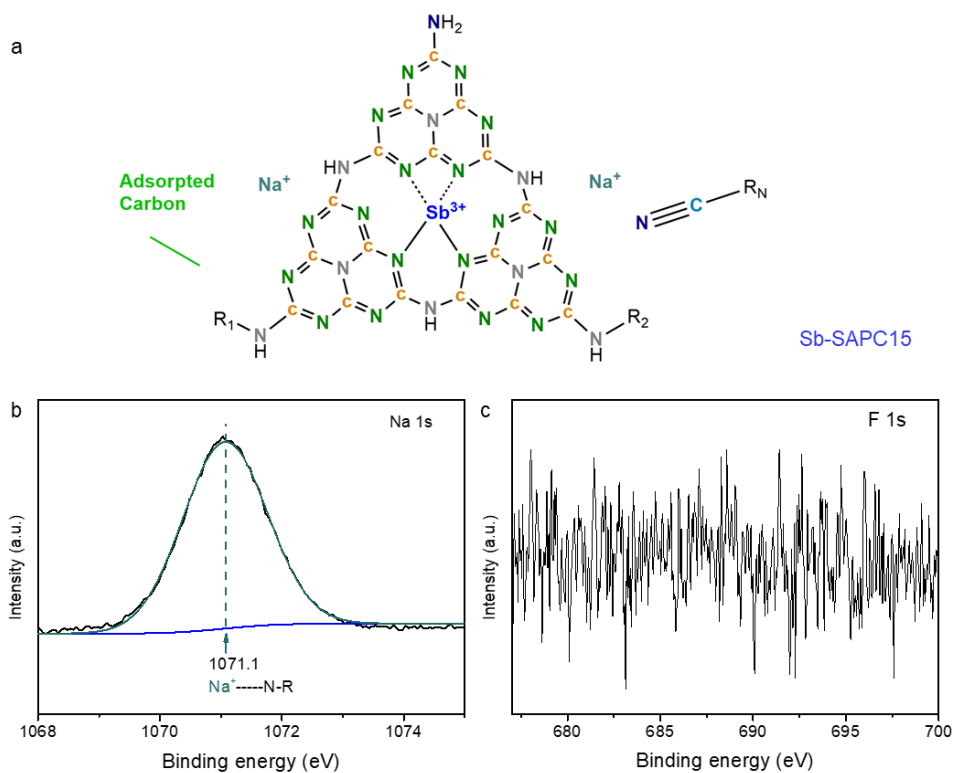
No edge could be detected at energy range of 685-695 eV of these 3 spectra, further suggesting no F in Sb-SAPC.



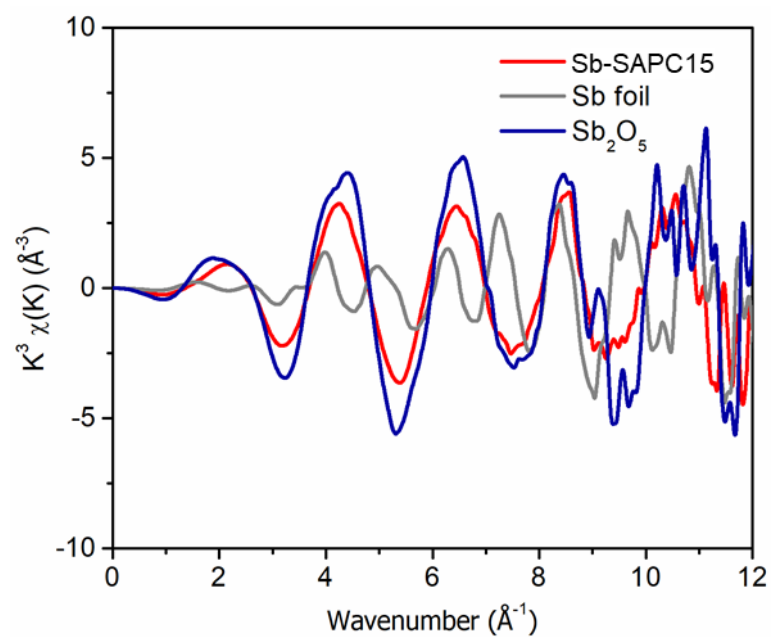
**Supplementary Figure 24 | FT-IR spectra of PCN samples and Sb-SAPCs.** **a**, FT-IR spectra of pristine PCN, PCN\_Na15, and Sb-SAPC15. **b**, FT-IR spectra of Sb-SAPC1, Sb-SAPC5, Sb-SAPC10 and Sb-SAPC15.



**Supplementary Figure 25 | Surface chemical states of PCN\_Na15.** **a**, Schematic diagram showing the chemical states of elements in PCN\_Na15. **b-e**, High-resolution XPS spectra of PCN\_Na15: C 1s (**b**); N 1s (**c**); Na 1s (**d**); and F 1s (**e**).

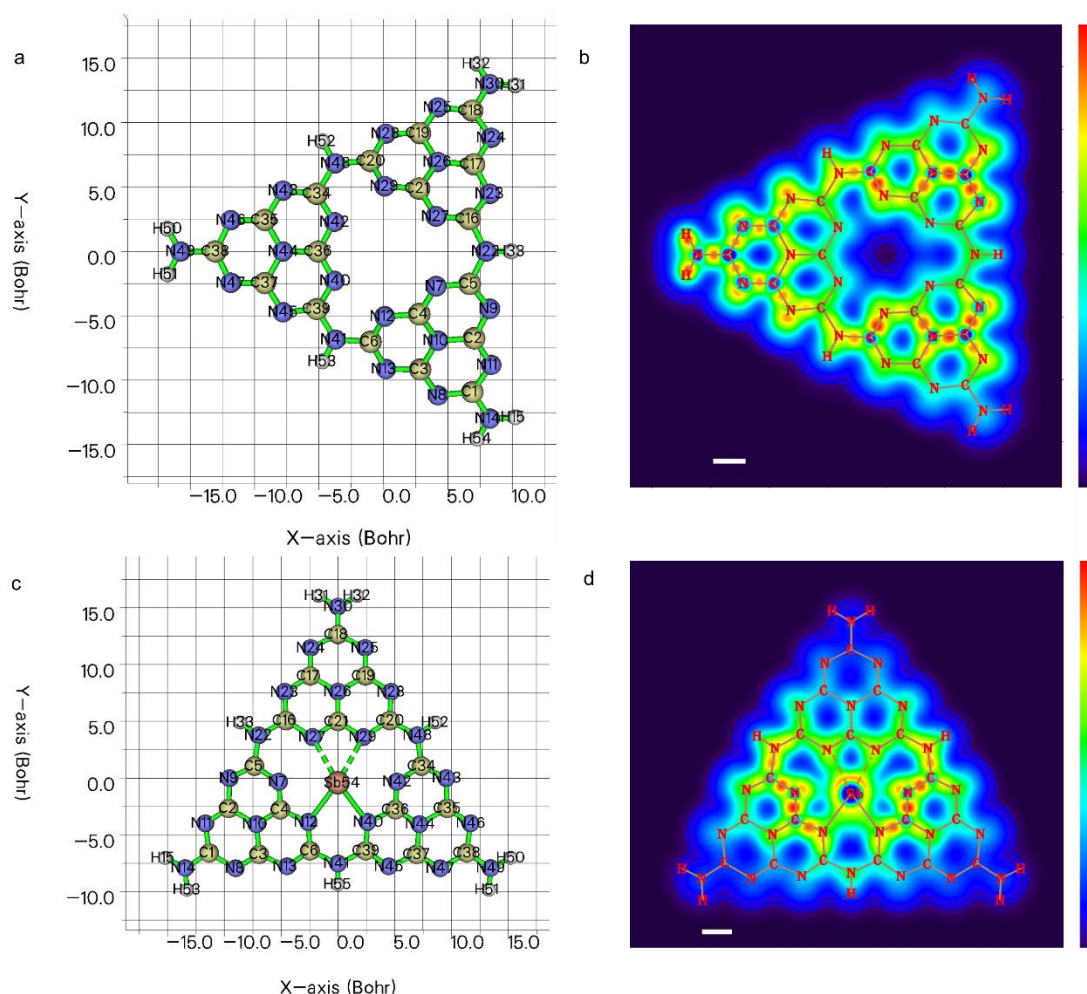


**Supplementary Figure 26 | Surface chemical states of Sb-SAPC15.** **a**, Schematic diagram showing the chemical states of elements in Sb-SAPC15. **b-c**, High-resolution XPS spectra of Sb-SAPC15: Na 1s (**b**) and F 1s (**c**).



**Supplementary Figure 27 | Extended X-ray absorption fine structure (EXAFS,  $k^3$ -weighted  $k$ -space) of Sb-SAPC15.** The spectrum of Sb-SAPC15 show a significant difference compared with references spectra (Sb foil and  $\text{Sb}_2\text{O}_5$ ).

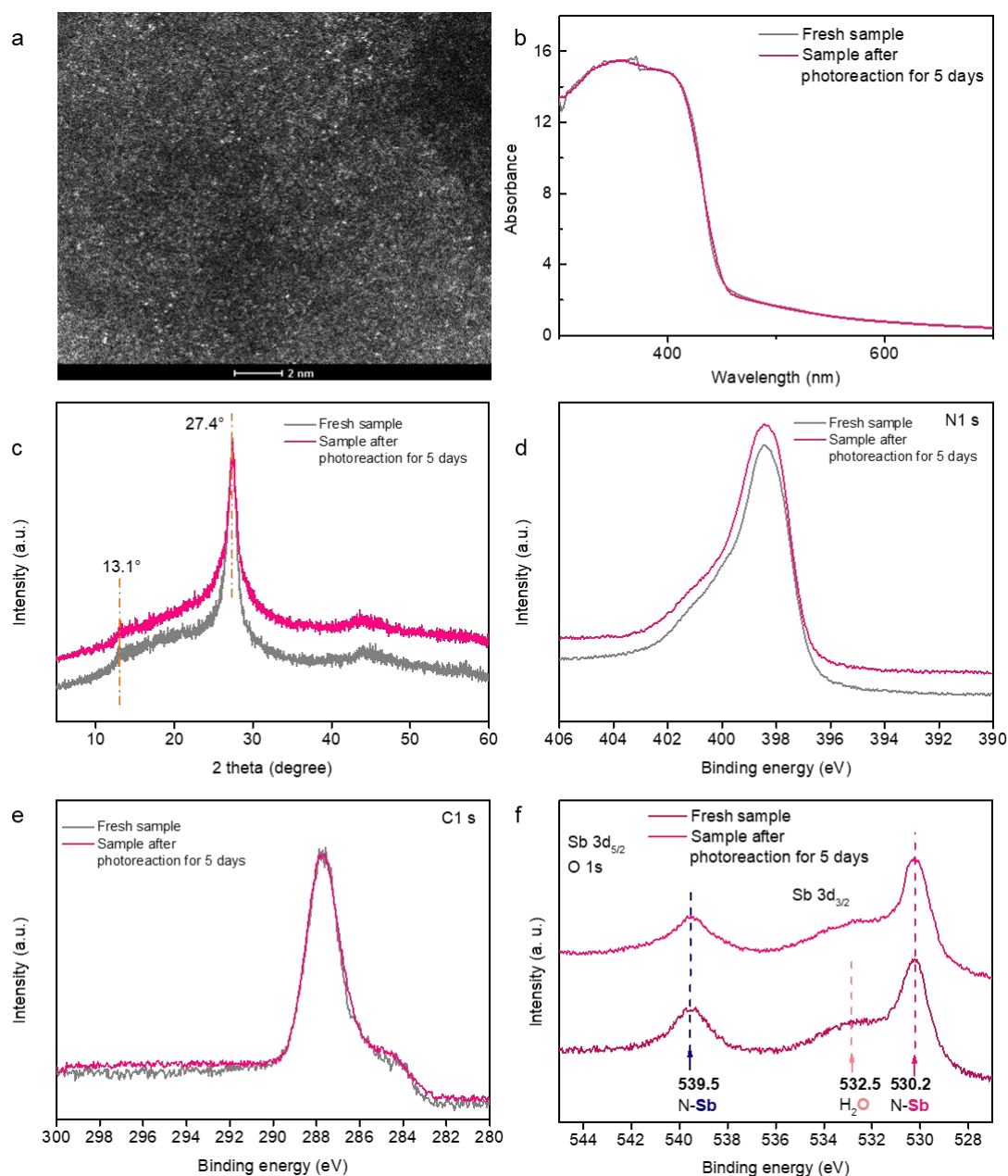




**Supplementary Figure 28 | Optimized geometry configuration and localized orbital locator of cluster models.** **a**, Optimized geometry configuration and atomic numbers of Melem\_3 to represent pristine PCN. **b**, Localized orbital locator calculated based on  $\pi$  MOs of melem\_3 (XY plane,  $Z = 0.45$  Bohr). **c**, Optimized geometry configuration and atomic numbers of melem\_3Sb3+ to represent Sb-SAPCs. **d**, Localized orbital locator calculated based on  $\pi$  MOs of melem\_3Sb3+ (XY plane,  $Z = 1.2$  Bohr). The dashed bonds refer to the weak interaction between N and Sb atoms. The scale bars in **(b)** and **(d)** are 5 Bohr. The maximum and minimum electronic density in **(b)** and **(d)** are 0.00 and 0.75.

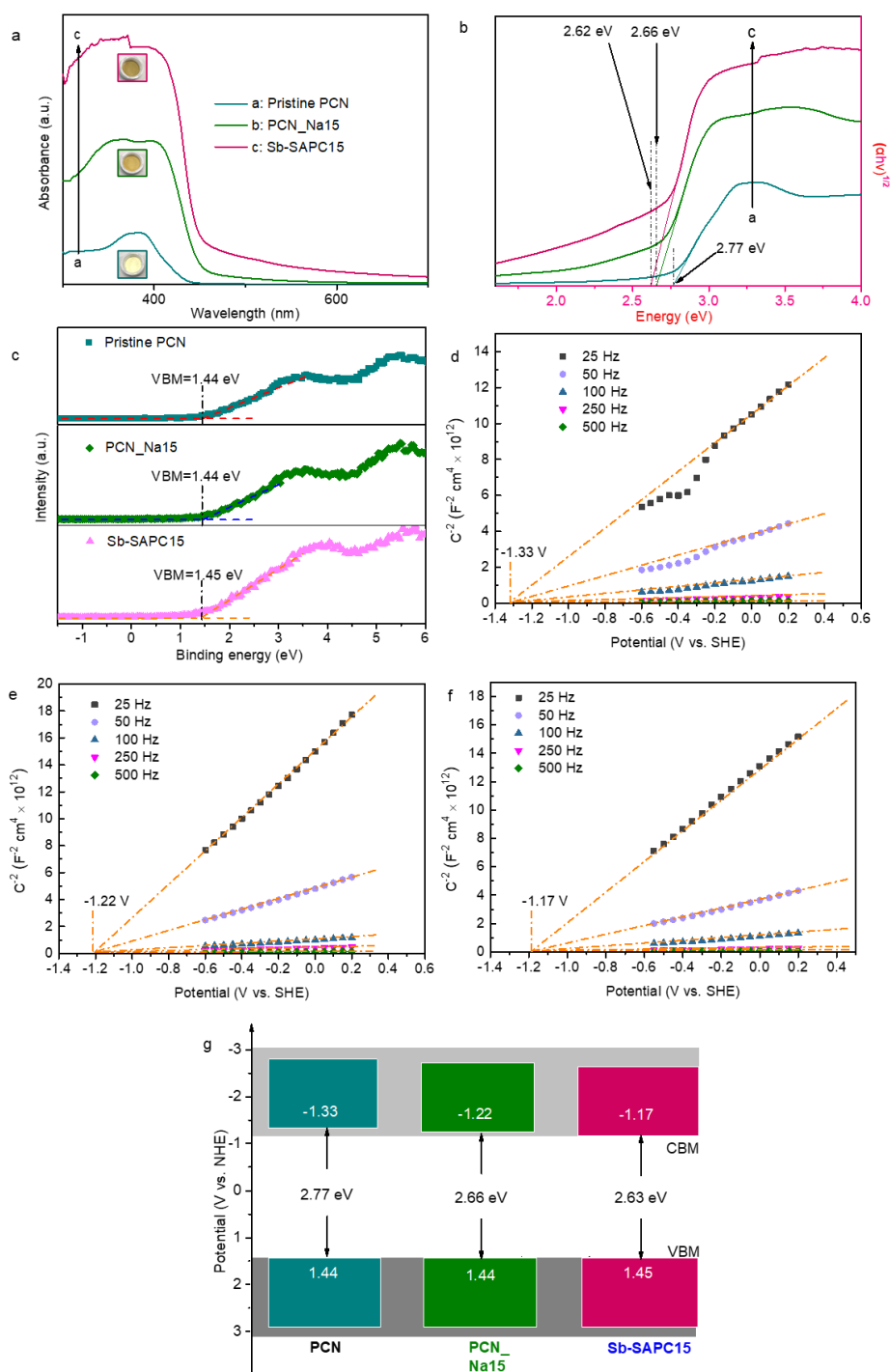
As shown in Supplementary Figure 28c & d, the sum of occupied  $\pi$  MOs at N12 and N40 strongly interacts with that at Sb54, thus two strong covalent bonds can be formed. Additionally, the sum of occupied  $\pi$  MOs at N27 and N28 also interacts with that at Sb54. The summed electronic intensity between N27 and Sb54 (as well as N28 and Sb54) is slightly weaker than that between N12 and Sb54 (as well as N40 and Sb54), indicating the slightly weaker interaction between N27 and Sb54 (Supplementary Figure 28d). These results further manifest the best fitting result for the first shell that each Sb atom is coordinated with about 3.3 N atoms in average (Figure 2h).



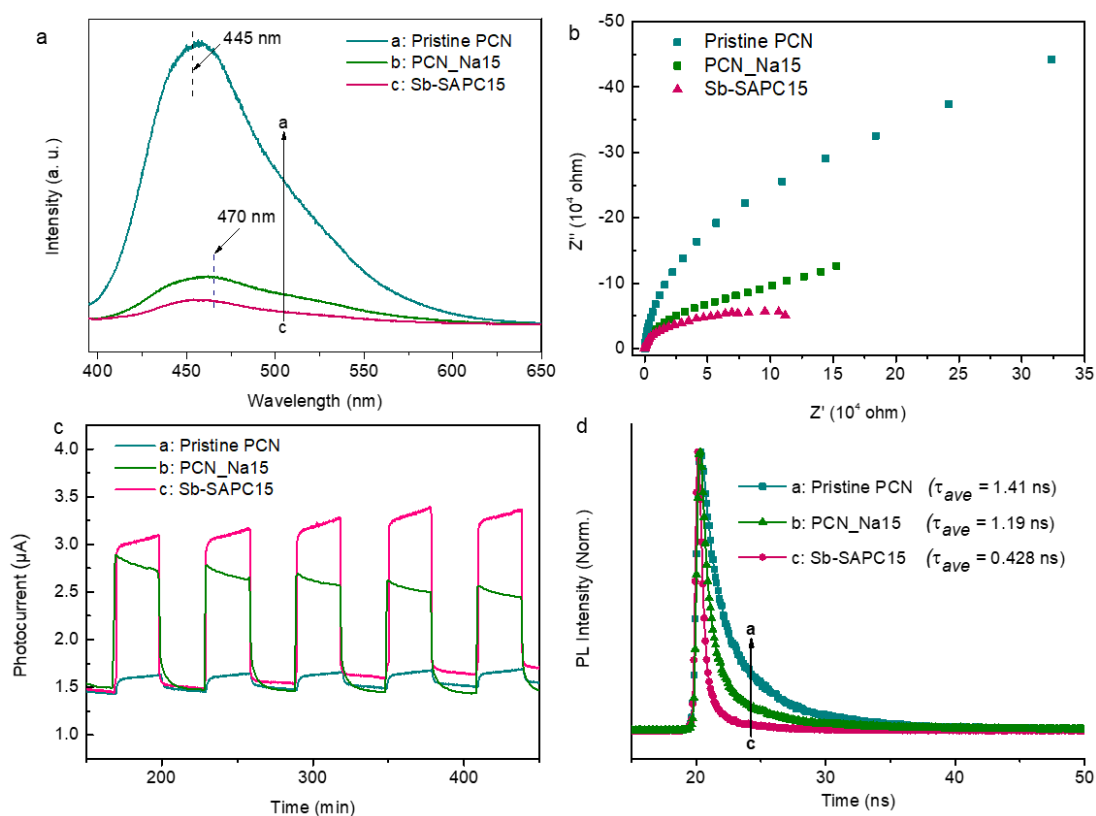


**Supplementary Figure 29 | Post-characterization of Sb-SAPC15 after photocatalysis.**

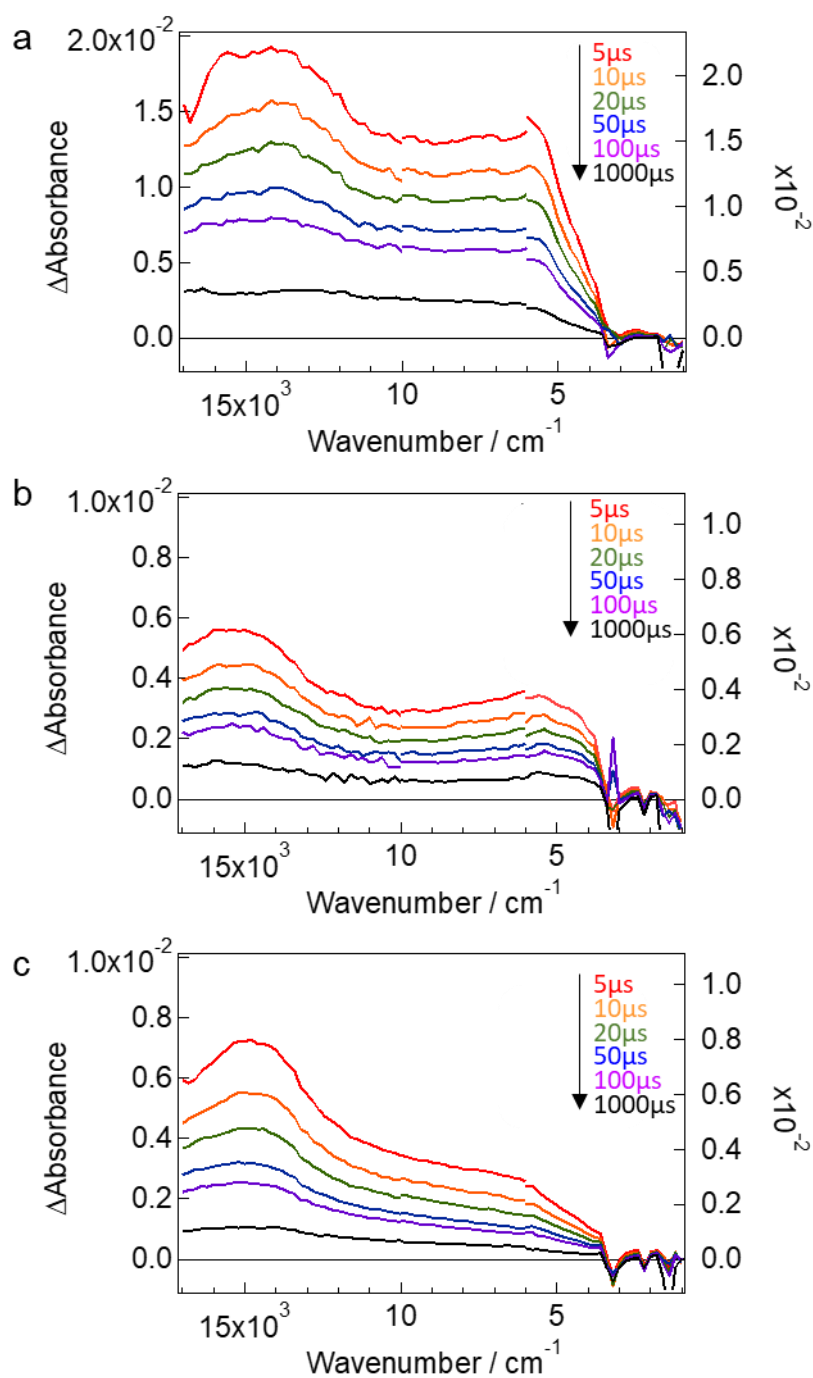
**a**, HAADF STEM image of Sb-SAPC15 after 5 days of photoreaction. **b-f**, Comparison of as-prepared Sb-SAPC15 and Sb-SAPC15 after 5 days of photoreaction: **(b)** UV-vis spectra; **(c)** XRD pattern; **(d)** high resolution XPS N 1s spectra; **(e)** high resolution XPS C 1s spectra; and **(f)** high resolution XPS O 1s and Sb 3d XPS spectra. After every 8 h of reaction, the reaction solution was exchanged by fresh 0.1 M phosphate buffer solution saturated with O<sub>2</sub>. Light intensity: 30.3 W m<sup>-2</sup> at 420-500 nm.



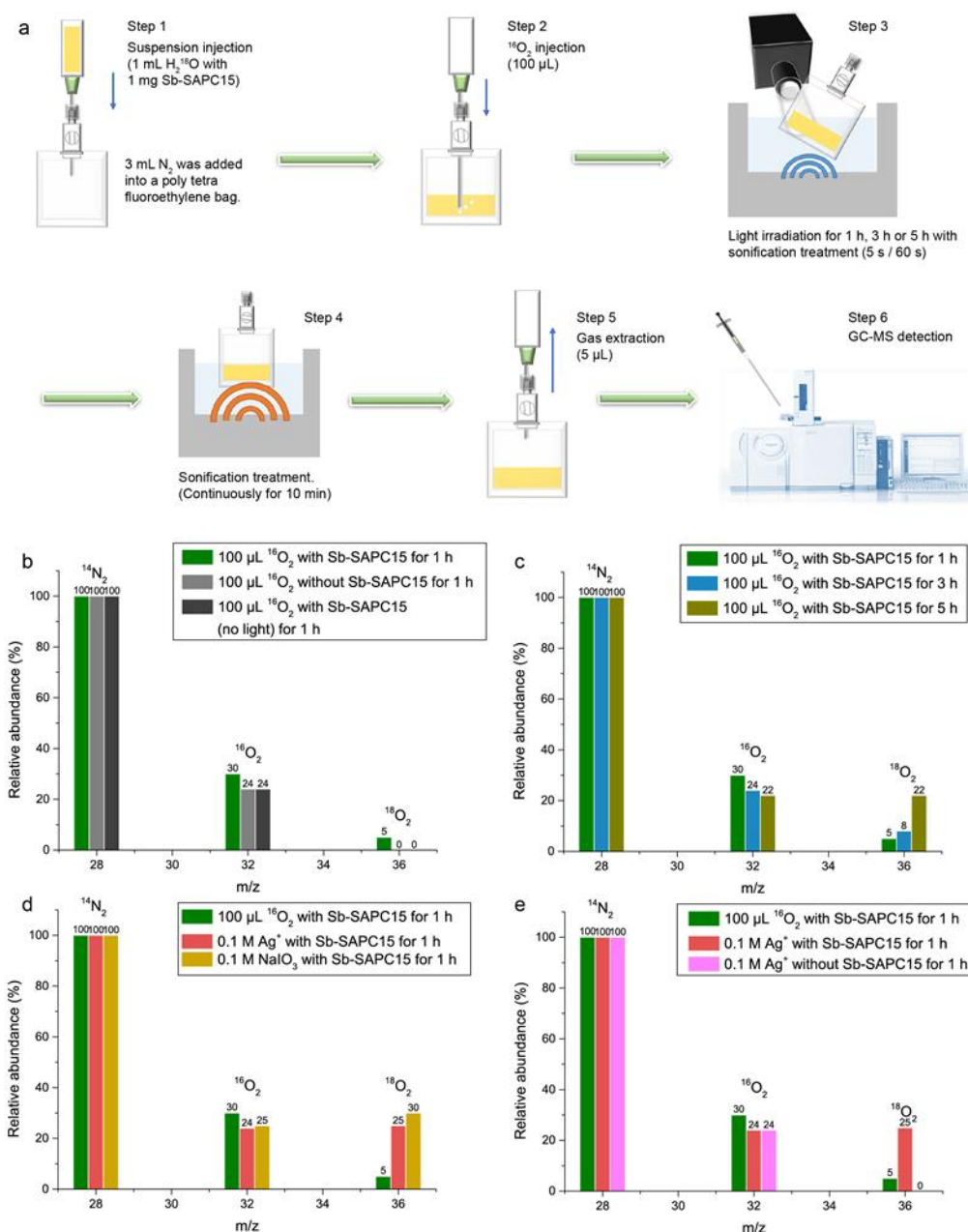
**Supplementary Figure 30 | Characterization of the CBM and VBM.** **a**, UV-vis diffuse reflection spectra of pristine PCN, PCN<sub>Na15</sub> and Sb-SAPC15. **b**, Tauc plot of pristine PCN, PCN<sub>Na15</sub> and Sb-SAPC15. **c**, Valence-band XPS spectra of pristine PCN, PCN<sub>Na15</sub> and Sb-SAPC15. **d-f**, Mott Schottky plots of (**d**) pristine PCN, (**e**) PCN<sub>Na15</sub> and (**f**) Sb-SAPC15. **g**, Band structure diagrams of PCN, PCN<sub>Na15</sub> and Sb-SAPC15. The Fermi level of the instrument (VB-XPS) is equilibrated at 4.5 eV utilizing Au metal basis as the reference. In this case, the numerical value of the binding energy in the calibrated VB-XPS spectrum is the same as the potential vs. normal hydrogen electrode.



**Supplementary Figure 31 | Evaluation of charge separation.** **a**, Photoluminescence spectra of PCN, PCN\_Na15 and Sb-SAPC15 at an excitation wavelength of 380 nm. **b**, Electrochemical impedance spectroscopy (EIS) spectra (Nyquist plots) of pristine PCN and Sb-SAPC15 in the frequency range from 100 kHz to 0.01 Hz at 0.6 V (vs. Ag/AgCl) under visible light irradiation. **c**, Comparison of photocurrent response between pristine PCN and Sb-SAPC15 at -0.6 V (vs. Ag/AgCl) under visible light illumination. The light source used in the EIS and photocurrent measurement is a Xe lamp with a UV cut ( $\lambda > 420$  nm) filter (light intensity at 420–500 nm:  $30.3 \text{ W m}^{-2}$ ). **d**, Time-resolved photoluminescence spectra of pristine PCN, PCN\_Na15 and Sb-SAPC15 recorded at 25 °C. The electrolyte used for the EIS and photocurrent measurement is 0.1 M phosphate buffer (pH = 7.4).

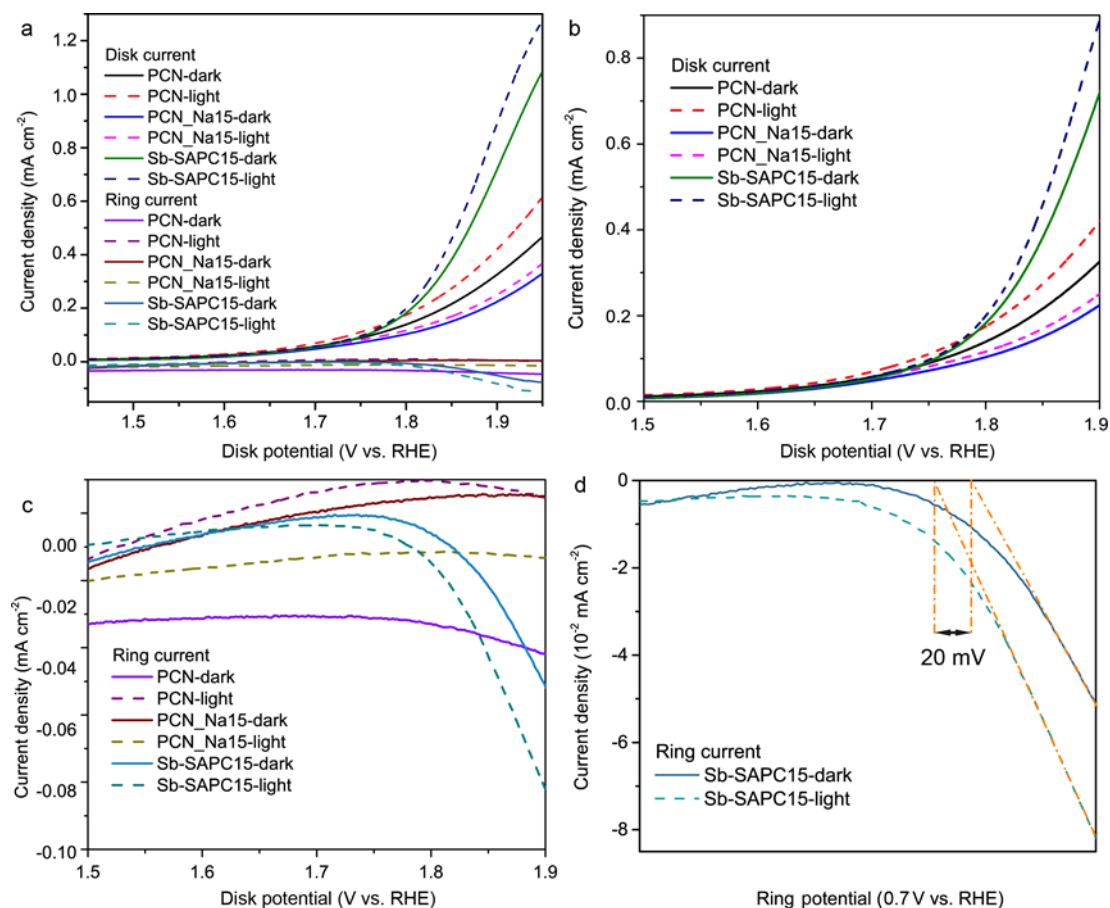


**Supplementary Figure 32 | Transient infrared red (IR) absorption spectra. a-c,** Transient IR absorption spectra for PCN (a), PCN\_Na15 (b) and Sb-SAPC15 (c) evolved after 420 nm laser pulse excitation under vacuum (6 ns, 5 mJ, 5 Hz).

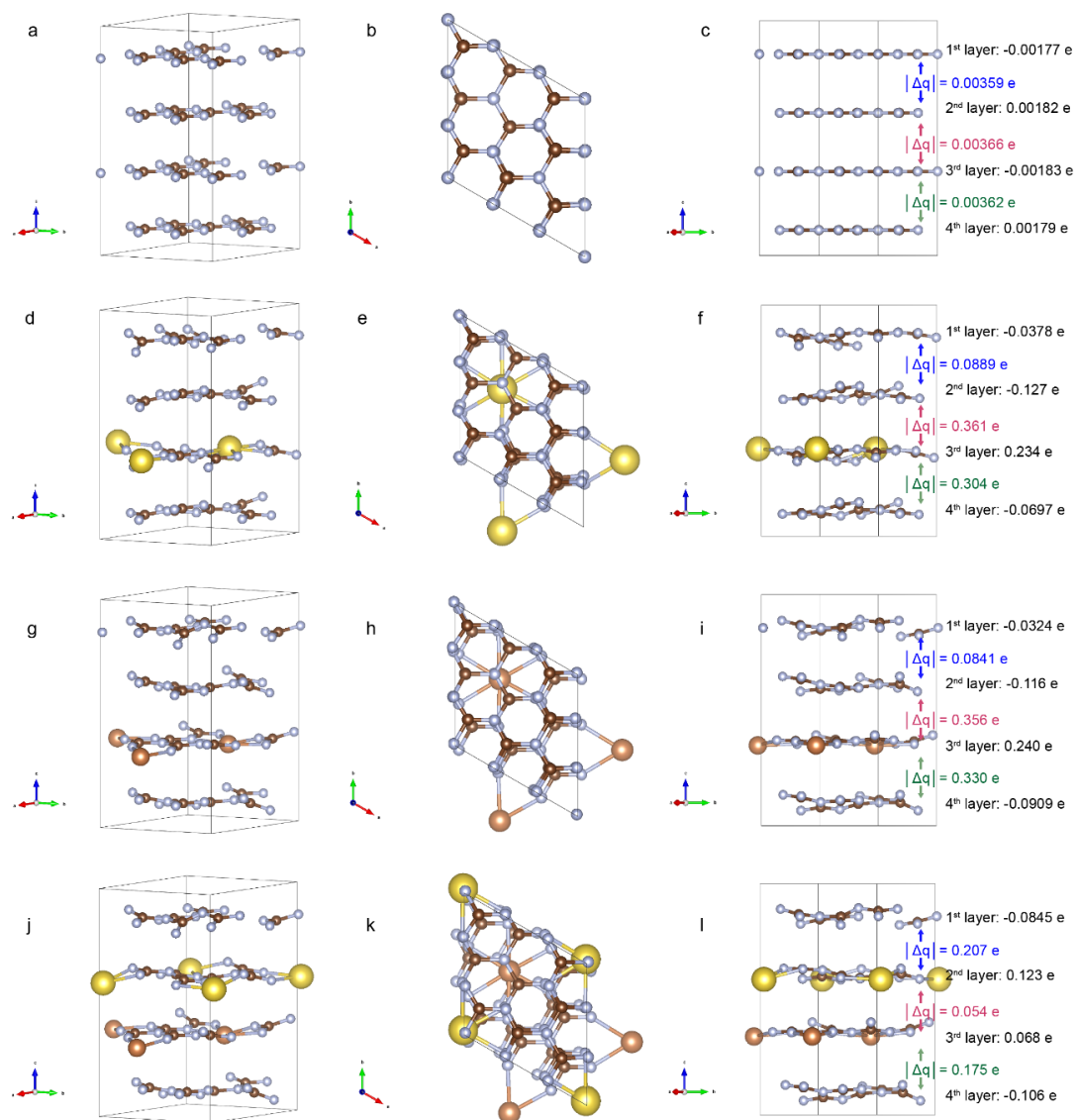


**Supplementary Figure 33 | Water oxidation mechanism. a**, Schematic diagram showing the isotopic experiment for H<sub>2</sub>O<sub>2</sub> production with addition of <sup>16</sup>O<sub>2</sub> as the electron acceptor and H<sub>2</sub><sup>18</sup>O as the electron donor (The figure of GC-MS in step 7 is taken from <https://www.an.shimadzu.co.jp/gcms/2010se.htm>). **b**, GC-MS spectra of the gas extracted from the Sb-SAPC15 system with <sup>16</sup>O<sub>2</sub> as the electron acceptor and H<sub>2</sub><sup>18</sup>O as the electron donor. Control experiments without addition of Sb-SAPC15 or without light irradiation were conducted for confirming the photo-induced oxygen generation reaction. **c**, GC-MS spectra of the gas extracted from the Sb-SAPC15 system after Xenon lamp illumination of 1 h, 3 h and 5 h in step 3. **d**, GC-MS spectra of the gas extracted from the Sb-SAPC15 system with different electron acceptors (100 μL O<sub>2</sub>, 0.1 M Ag<sup>+</sup> or 0.1 M NaIO<sub>3</sub>). **e**, GC-MS spectra of the gas extracted from the system with or without addition of Sb-SAPC in condition of adding different electron acceptors (100 μL O<sub>2</sub> or 0.1 M Ag<sup>+</sup>).

With increasing irradiation time, the signal of  $^{18}\text{O}_2$  ( $m/z = 36$ ) gradually increased (Supplementary Figure 33c). Additionally, we also investigated the oxygen generation with addition of other electron acceptors (0.1 M  $\text{Ag}^+$  or 0.1 M  $\text{NaIO}_3$ ). The signal of  $^{18}\text{O}_2$  ( $m/z = 36$ ) significantly increased after addition of silver ion or  $\text{NaIO}_3$  compared to the case with injection of 100  $\mu\text{L}$   $^{16}\text{O}_2$  (Supplementary Figure 33d), indicating that both of silver ion and  $\text{NaIO}_3$  could serve as efficient sacrificial reagent for oxygen evolution. To investigate whether the  $\text{Ag}^+$  could directly produce oxygen or work as the sacrificial reagent, we conducted a control experiment with Ag in solution. As shown in Supplementary Figure 33e, the signal of  $^{18}\text{O}_2$  ( $m/z = 36$ ) could not be detected without the addition of photocatalyst, indicating that pure  $\text{Ag}^+$  in the system could not produce  $\text{O}_2$ , which suggests that the  $\text{Ag}^+$  just serves as a sacrificial reagent for photocatalytic WOR.

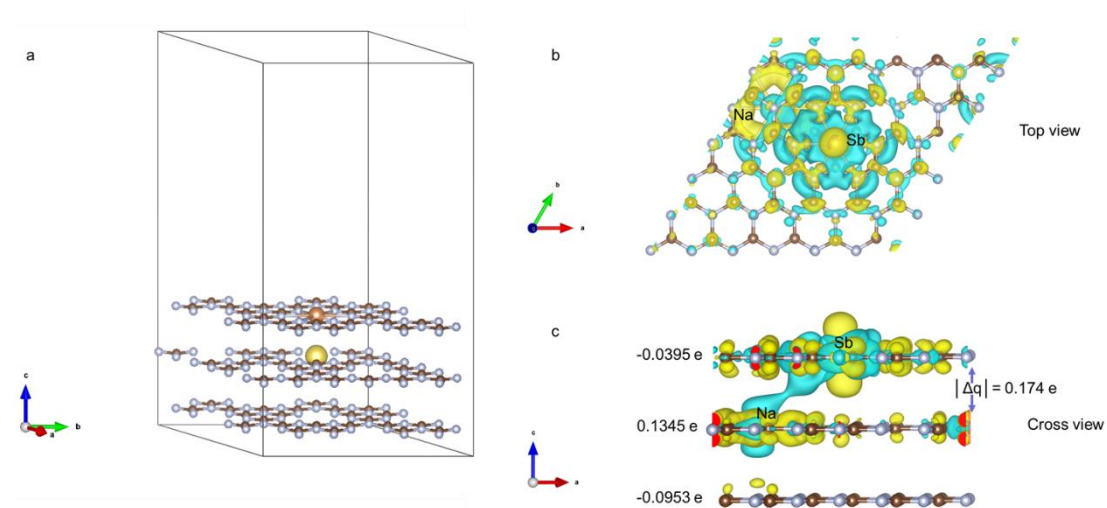


**Supplementary Figure 34 | The anodic polarization curves of rotating ring disk electrode modified by PCN, PCN\_Na15 and Sb-SAPC15 with or without light irradiation.** **a**, Comparison of the anodic polarization curves of the rotating ring disk electrode PCN, PCN\_Na15 and Sb-SAPC15 irradiated by light or in the dark condition. **b**, Anodic polarization curves of the rotating disk electrode PCN, PCN\_Na15 and Sb-SAPC15 in dark condition or with light irradiation. **c**, Anodic polarization curves of the ring electrode PCN, PCN\_Na15 and Sb-SAPC15 with light irradiation or in absence of light. **d**, Enlarged ring current of rotating ring disk electrode modified by Sb-SAPC15. The disk potential was shifted from 1.4 to 1.95 V (vs. RHE), and the potential of the ring was set at 0.7 V (vs. RHE). In this case, the signal of O<sub>2</sub> reduction to H<sub>2</sub>O (0.7 V vs. RHE) could be immediately captured by the ring electrode if O<sub>2</sub> was generated by water oxidation reaction. Solution: 0.1 M KOH aqueous solution (pH = 12.9).

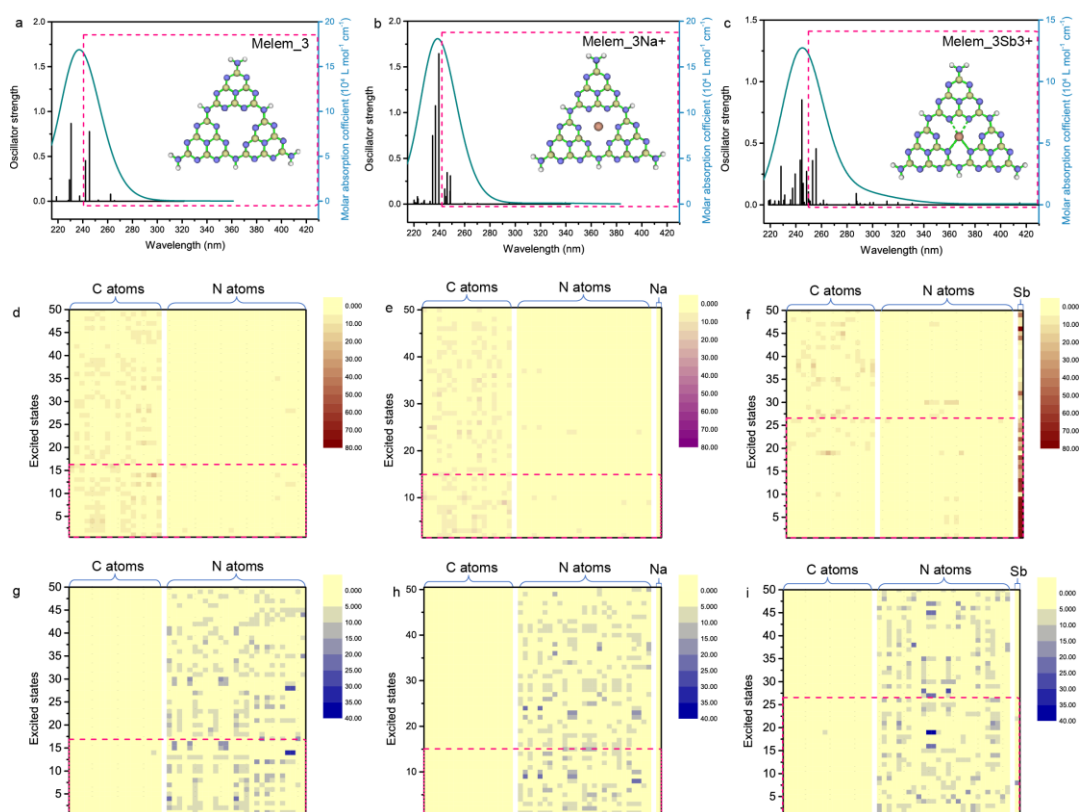


**Supplementary Figure 35 | Bader Charge distribution analysis from density functional theory (DFT) calculations. a-l, Charge distribution of pristine GCN (a-c), Na-GCN (d-f), Sb-GCN (g-i), and NaSb-GCN (j-l).  $|\Delta q|$  represents the absolute value of the difference of the electron distribution between the layers.**

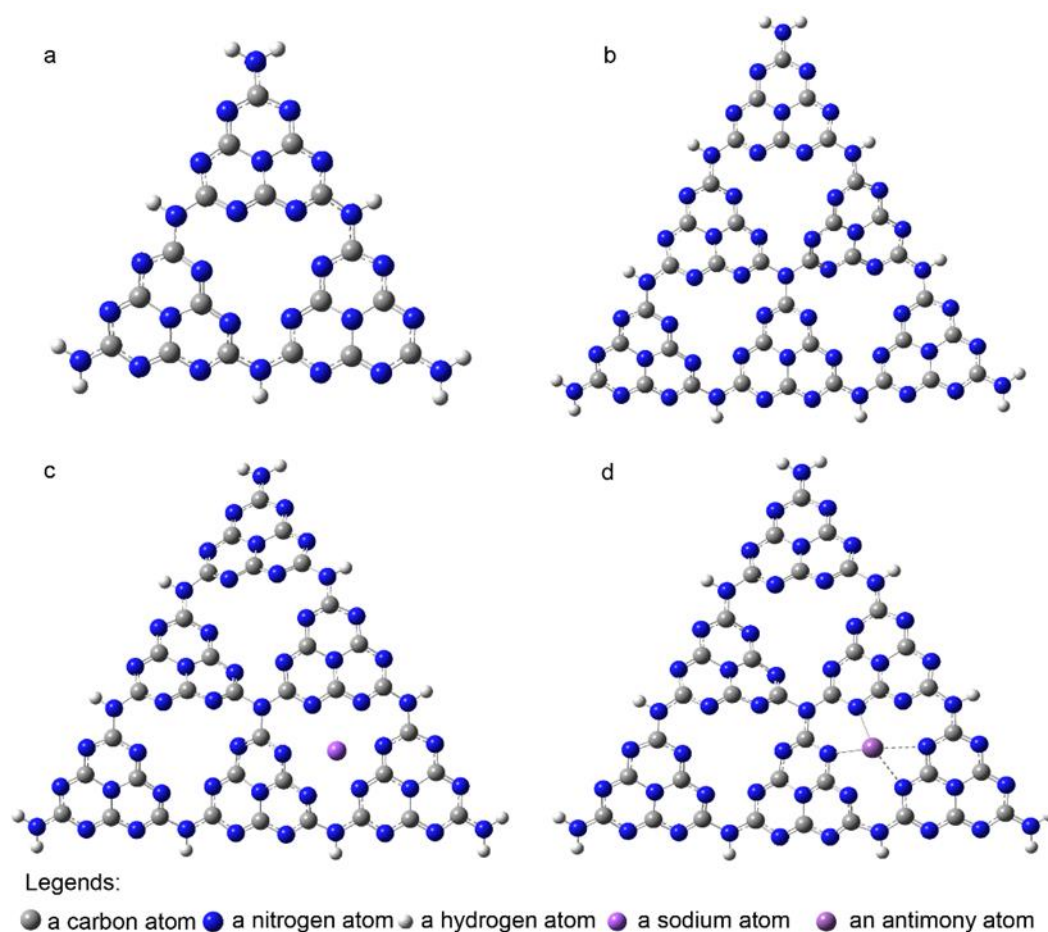




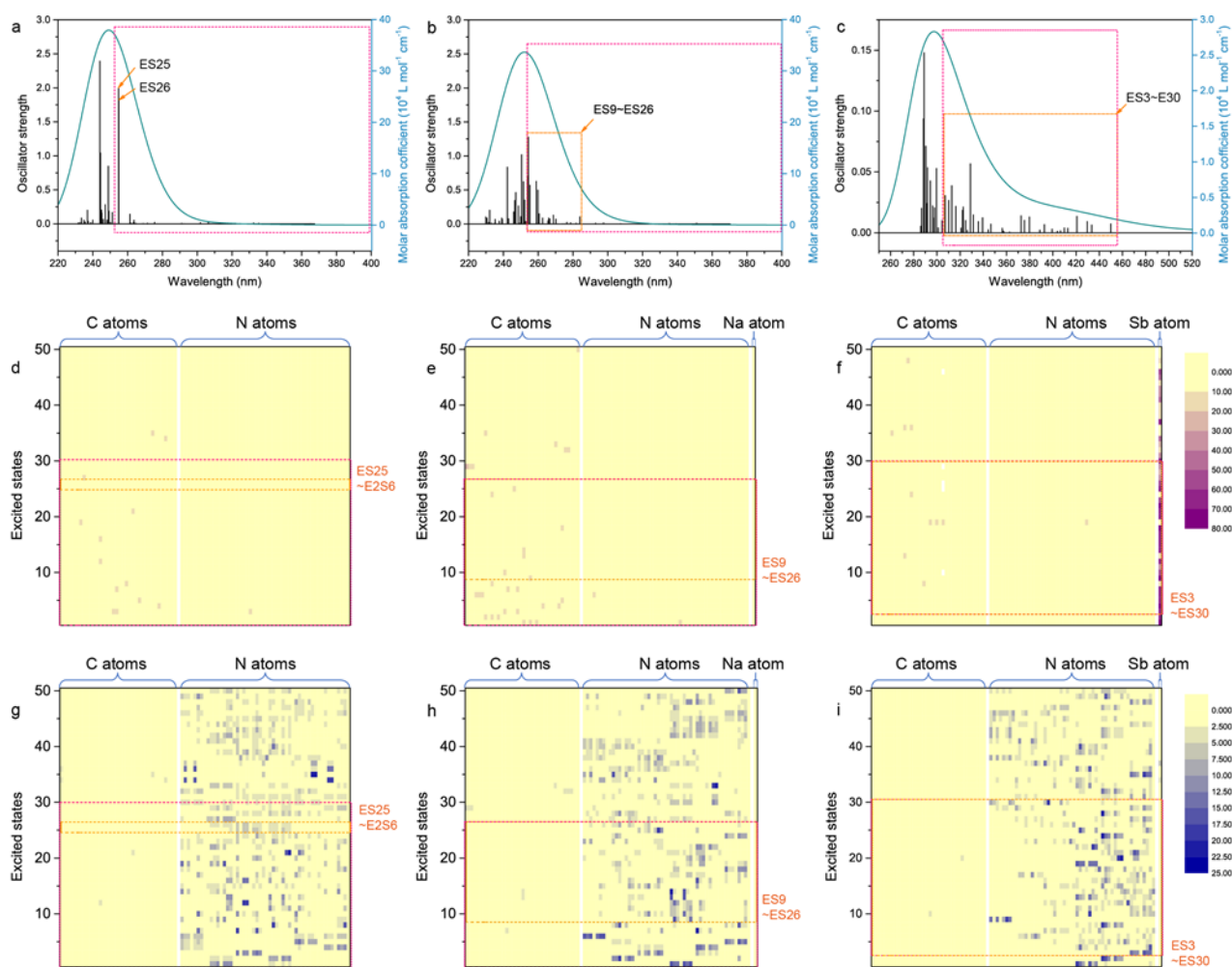
**Supplementary Figure 36 | Charge distribution analysis near surface of NaSb-GCN from density functional theory (DFT) calculations.** **a**, Optimized near surface crystal structure of NaSb-GCN. **b-c**, Enlarged top view (**b**) and cross view (**c**) of NaSb-GCN.  $|\Delta q|$  represents the absolute value of the difference of electron distribution between the first and second layer. Yellow color represents electron accumulation and blue color represents electron depletion.



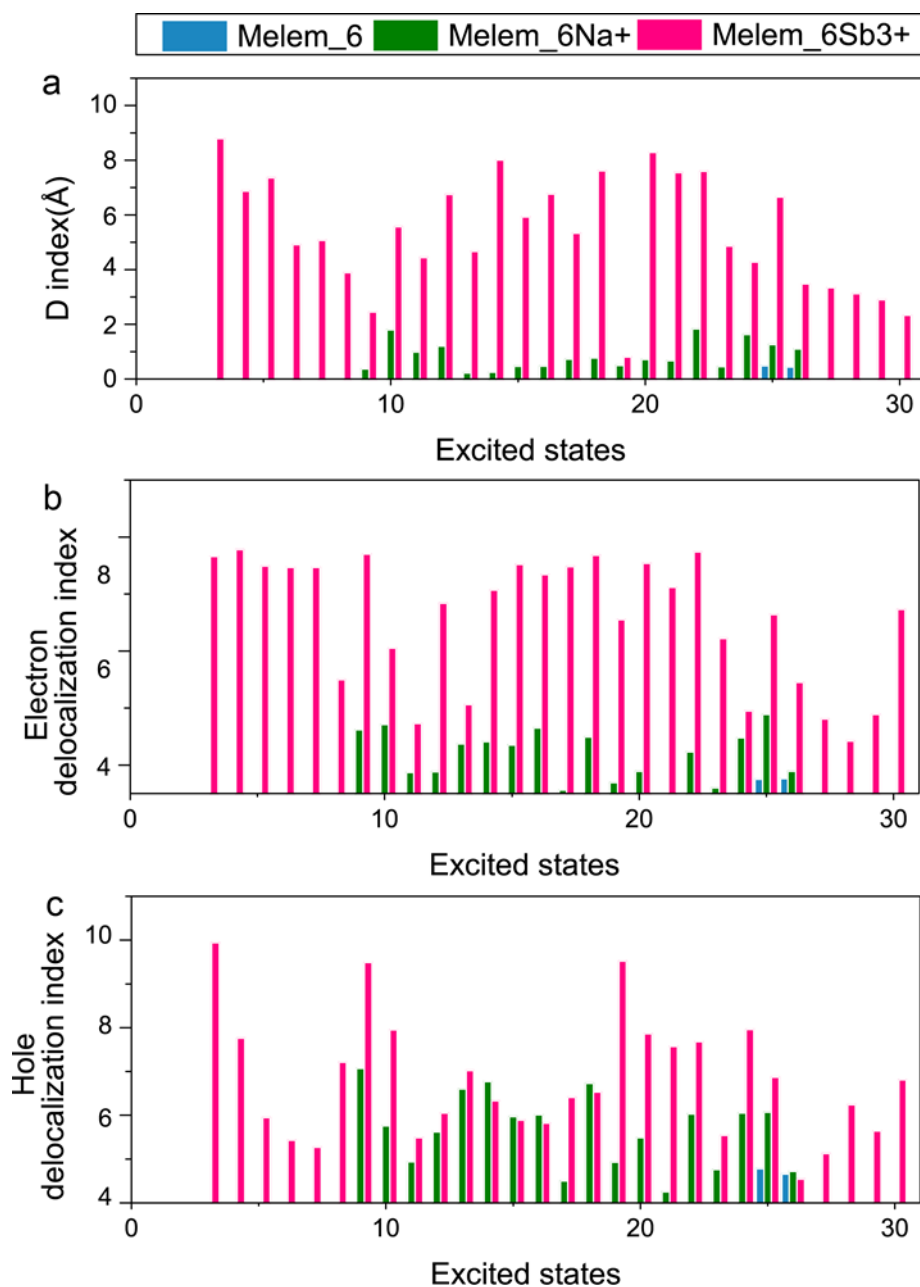
**Supplementary Figure 37 | Simulated excitation properties of Melem\_3, Melem\_3Na+ and Melem\_3Sb3+.** **a-c**, TDDFT-calculated absorption spectra for **(a)** Melem\_3, **(b)** Melem\_3Na+ and **(c)** Melem\_3Sb3+. **d-i**, The population of electron and hole distribution (vertical excitation at the excited states 1-50). **(d)** Electron distribution and **(g)** hole distribution for Melem\_3. **(e)** Electron distribution and **(h)** hole distribution for Melem\_3Na+. **(f)** Electron distribution and **(i)** hole distribution for Melem\_3Sb3+. The magenta dash circles are the excited states that possibly participate in the photocatalytic  $\text{H}_2\text{O}_2$  production.



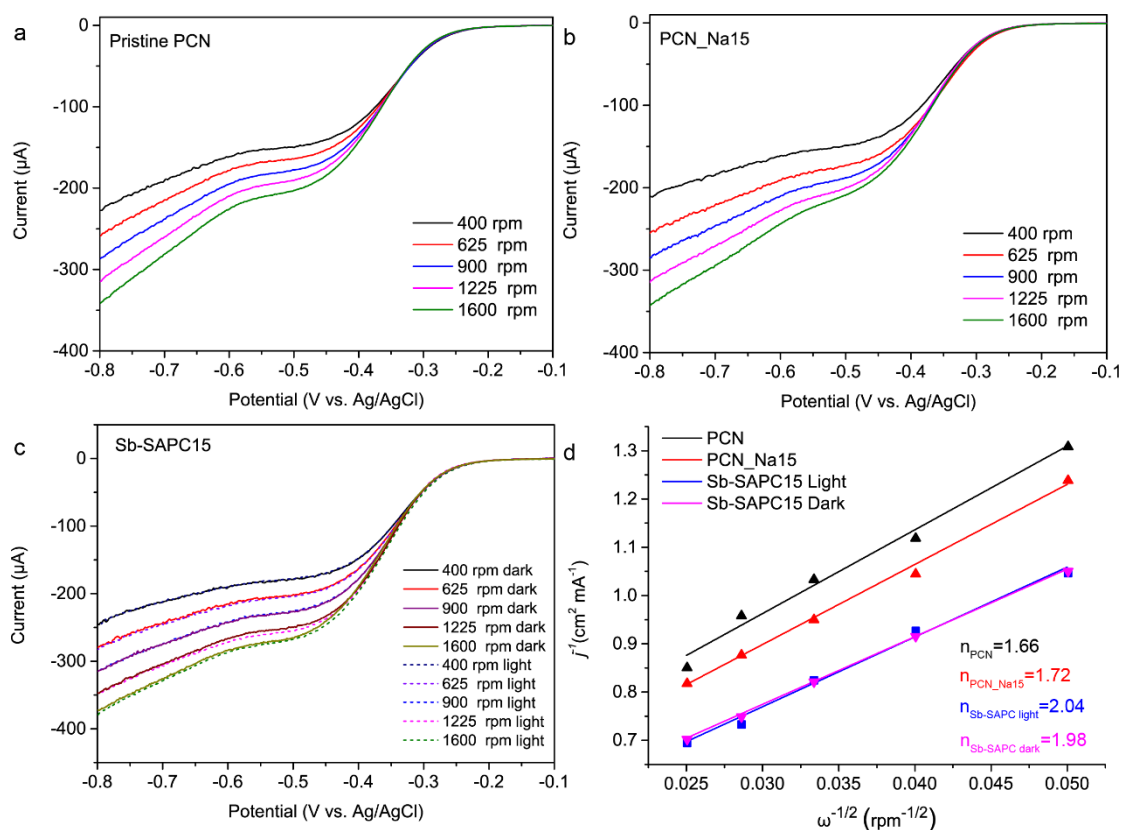
**Supplementary Figure 38 | Cluster models for investigating charge separation properties.** **a**, A cluster model for representing Melem\_3. **b**, Melem\_6 for representing PCN. **c**, Melem\_6Na<sup>+</sup> for representing sodium ion incorporated PCN. **d**, Melem\_6Sb<sup>3+</sup> for representing single atomic Sb incorporated PCN.



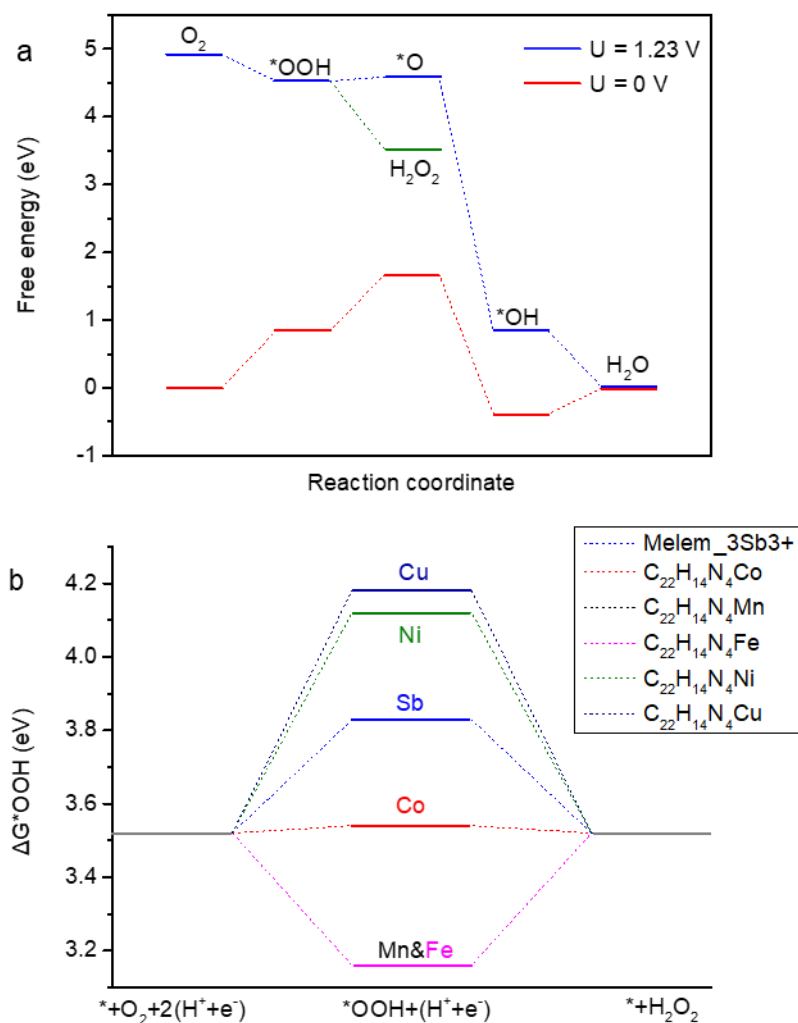
**Supplementary Figure 39 | Simulated excitation properties of Melem\_6, Melem\_6Na<sup>+</sup> and Melem\_6Sb<sub>3</sub><sup>+</sup>.** **a-c**, TDDFT-calculated absorption spectra for **(a)** Melem\_6, **(b)** Melem\_6Na<sup>+</sup> and **(c)** Melem\_6Sb<sub>3</sub><sup>+</sup>. **d-i**, The population of electron and hole distribution (vertical excitation at the excited states 1-50). **(d)** Electron distribution and **(g)** hole distribution for Melem\_6. **(e)** Electron distribution and **(h)** hole distribution for Melem\_6Na<sup>+</sup>. **(f)** Electron distribution and **(i)** hole distribution for Melem\_6Sb<sub>3</sub><sup>+</sup>. The magenta dash circles are the excited states that possibly participate in the photocatalytic H<sub>2</sub>O<sub>2</sub> production. The orange dash circles represent the most important transitions that contribute the most for the spectra for photocatalytic H<sub>2</sub>O<sub>2</sub> production.



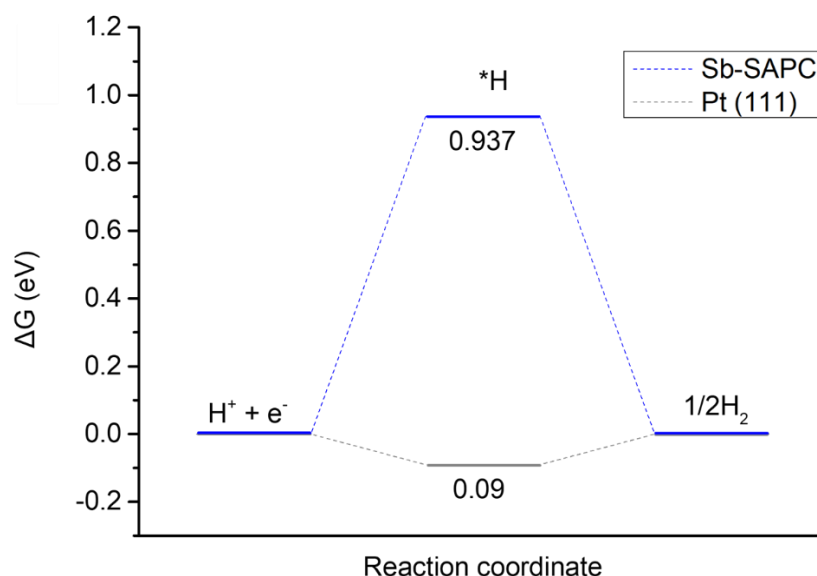
**Supplementary Figure 40 | Simulated properties of Melem\_6, Melem\_6Na+ and Melem\_6Sb3+ for charge separation and the localization of electrons and holes. a,** D index of the transitions of ES25 and ES26 of Melem\_6, ES9~ES26 of Melem\_6Na+ and ES3~ES30 of Melem\_6Sb3+. **b-c,** Delocalization index of (b) electrons and (c) holes for the transitions of ES25 and ES26 of Melem\_6, ES9~ES26 of Melem\_6Na+ and ES3~ES30 of Melem\_6Sb3+.



**Supplementary Figure 41 | Investigation of electron transfer numbers.** **a-b**, Linear sweep voltammetry (LSV) curves of pristine PCN (**a**) and Sb-SAPC15 (**b**) recorded on a rotating disk glassy carbon electrode in 0.1 M KOH saturated with O<sub>2</sub> in dark condition. **c**, Linear sweep voltammetry (LSV) curves of Sb-SAPC15 recorded on a rotating disk glassy carbon electrode in 0.1 M KOH saturated with O<sub>2</sub> under dark or visible light illumination. **d**, Koutecky–Levich plots (at -0.6 V vs. Ag/AgCl).



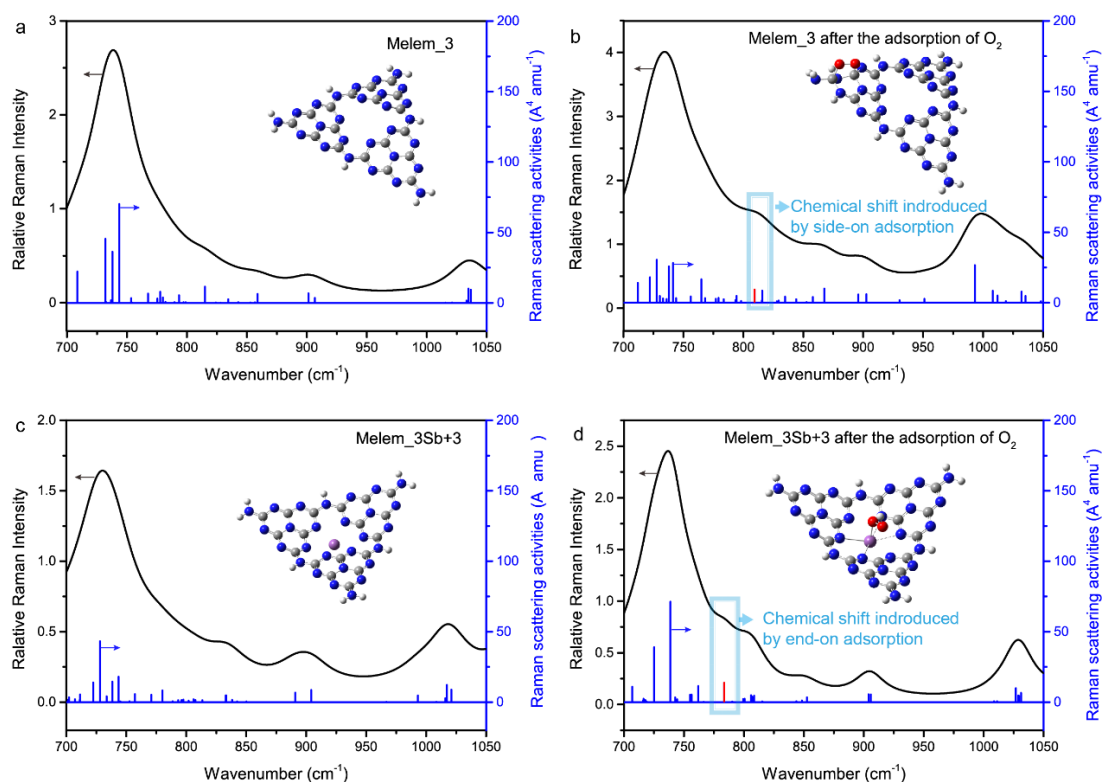
**Supplementary Figure 42 | Energetic diagram for ORR.** **a**, Calculated free energy diagrams at  $U = 0$  (blue line) and  $U = 1.23\text{ V}$  (red line) vs. RHE for  $2e^-$  (green line) and  $4e^-$  ORR on Melem\_3Sb3+. **b**, Comparison of  $\Delta G^*_{OOH}$  for the  $2e^-$  ORR on Sb-SAPC15 and  $C_{40}H_{16}N_4M$ ,  $M = Mn, Fe, Co, Ni$ , and  $Cu$  at  $U = 0.7\text{ V}$  vs. RHE. The free energy diagram of  $C_{40}H_{16}N_4M$  is adopted from our previous report<sup>2</sup>.



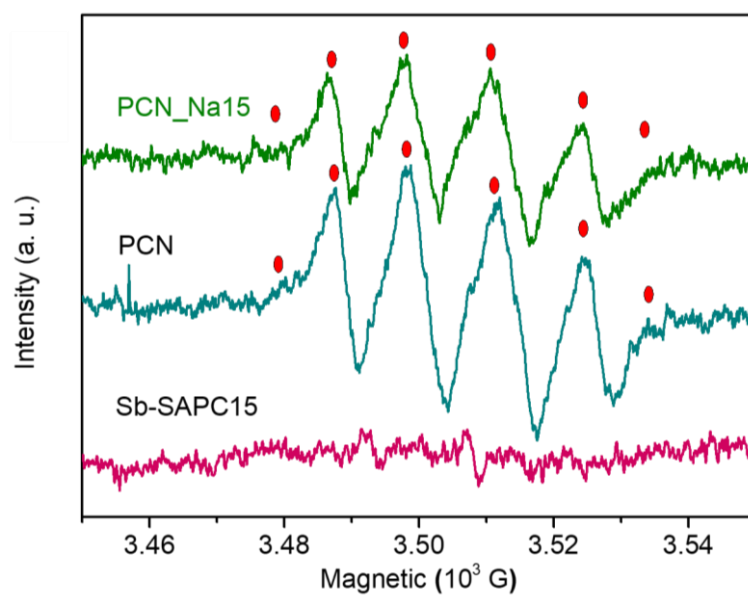
**Supplementary Figure 43 | Interaction of hydrogen atoms and Sb sites and energetic diagram for HER.** Comparison of  $\Delta G_{*H}$  for HER on Melem\_3Sb3+ and Pt (111).

The interaction of hydrogen atoms and Sb sites is weak for the following reasons: (1) A typical Sb-H bonding exists in  $SbH_3$ . The oxidation number of Sb in  $SbH_3$  is -3, whereas EXAFS fitting data shows that the chemical state of Sb sites in Sb-SAPC is close to +3. Thus, chemical bonding between Sb(+3) in Sb-SAPC and hydrogen is hardly believed. (2) The free energy diagram of Melem\_3Sb3+\*H is close to 1 eV, indicating that the adsorption of free H is quite hard on the Sb sites.





**Supplementary Figure 44 | Calculated Raman shift by using the function of  $\omega 97\text{xd}$  at 6-311g(d) level. a-b**, Simulated Raman spectra for (a) the tri-s-triazine units and the units with (b)  $^{16}\text{O}-^{16}\text{O}$  side-on species. **c-d**, Simulated Raman spectra for (c) the Sb-sites and the units with (d)  $^{16}\text{O}-^{16}\text{O}$  end-on species. The white, gray, blue, red, and purple spheres represent H, C, N, O and Sb atoms, respectively.



**Supplementary Figure 45 | ESR spectra of PCN, PCN\_Na15 and Sb-SAPC15 recorded in methanol solution using 5,5-dimethyl-1-pyrroline N-oxide as a radical trapper.**

**Supplementary Table 1. Activity comparison between Sb-SAPC15 and other reported photocatalysts and photoelectrodes for non-sacrificial H<sub>2</sub>O<sub>2</sub> production.**

Photocatalytic system	Concentration of photocatalyst	Irradiation condition	H <sub>2</sub> O <sub>2</sub> yield	AQE/ SCC efficiency	Ref.
g-C <sub>3</sub> N <sub>4</sub> /PDIx	1.7 mg mL <sup>-1</sup>	λ > 420 nm	50.6 μmol (48 h)	2.5% at 420 nm/ NA	[3]
g-C <sub>3</sub> N <sub>4</sub> /PDI/RGO	1.7 mg mL <sup>-1</sup>	λ > 420 nm	38 μmol (2 h)	6.1% at 420 nm/ 0.2%	[4]
Graphene oxide	0.32 mg mL <sup>-1</sup>	λ > 420 nm	1.4 μmol (6 h)	NA/ NA	[5]
Si/TiO <sub>2</sub> -Au	-----	λ = 365 nm	40 μmol (75 h)	NA/ NA	[6]
TiO <sub>2</sub> -Pt	0.05 mg mL <sup>-1</sup>	Full spectrum	5.096 μmol (1 h)	NA/ NA	[7]
g-C <sub>3</sub> N <sub>4</sub> /MTI	1.7 mg mL <sup>-1</sup>	λ > 420 nm	27.5 μmol (24 h)	6.1% at 420 nm/ 0.18%	[8]
g-C <sub>3</sub> N <sub>4</sub> /PDI-BN-RGO	1.7 mg mL <sup>-1</sup>	λ > 420 nm	34 μmol (24 h)	7.3% at 420 nm/ 0.28%	[9]
Resorcinol– formaldehyde resins	1.7 mg mL <sup>-1</sup>	λ > 420 nm	99 μmol (24 h)	7.5% at 450 nm/ 0.5%	[1]
<b>Sb-SAPC15</b>	<b>2 mg mL<sup>-1</sup></b>	<b>λ &gt; 420 nm</b>	<b>470.5 μmol (8 h)</b>	<b>17.6% at 420 nm/ 0.61%</b>	<b>This work</b>

**Supplementary Table 2. Mass percentage of Sb in Sb-SAPCx.**

	Na mass percentage (%)	Substance amount of Na in 1 g catalyst (mmol)	Mass percentage of Sb (%)	Substance amount of Sb in 1 g catalyst (mmol)
PCN	0	0.00	0	0.00
PCN_Na15	2.00	0.87	0	0.00
Sb-SAPC0.5	0.08	0.03	0.63	0.05
Sb-SAPC1	0.16	0.07	0.96	0.08
Sb-SAPC3	0.44	0.19	2.28	0.19
Sb-SAPC5	0.72	0.31	4.31	0.36
Sb-SAPC10	1.18	0.51	7.85	0.65
Sb-SAPC15	1.51	0.66	10.88	0.90
PCN_Na15W*	2.01	0.87	0	0
Sb-SAPC15W*	1.50	0.65	10.85	0.89

\* PCN\_Na15W and Sb-SAPC15W indicate the samples washed by hot water (90 °C) for another 24 h.

We have tried to wash the as-prepared Sb-SAPC15 by hot water (90 °C) for extremely long time (24 hours) in order to remove the alkaline ions in the CN matrix<sup>10</sup>. However, the ICP result showed that the Na content kept almost constant after this treatment. The difficulty of removing Na in PCN by washing could be due to its existence nature. As revealed in the simulations based on DFT (both cluster model and periodic model), sodium tends to bond onto the matrix of PCN. However, the introduction of Na into PCN only slightly enhanced its photocatalytic activity.

**Supplementary Table 3. Elemental analysis.**

Sample name	N %	C %	H %	Mass <sub>C</sub> /Mass <sub>N</sub>
PCN	60.7	33.7	2.01	55.5%
PCN_Na15	57.5	33.1	1.70	57.5%
Sb-SAPC1	59.5	33.1	1.90	55.7%
Sb-SAPC5	56.8	31.7	1.78	55.8%
Sb-SAPC10	54.0	30.3	1.66	56.2%
Sb-SAPC15	49.6	28.5	1.61	57.5%
Sb-SAPC20	45.5	26.9	1.57	59.1%

**Supplementary Table 4. Fitting parameters of EXAFS data.**

Sample	Shell	N	R/Å	$\Delta E$	Debye-Waller factor $\sigma^2$ (Å <sup>2</sup> )	R-factor
Sb <sub>2</sub> O <sub>5</sub>	Sb-O	4.2±0.20	1.96±0.007	7.85±1.04	0.003±0.001	0.02
Sb-SAPC	Sb-N	3.3±0.20	2.0±0.03	9.74±0.94	0.002±0.0009	0.018

Shell: scattering pathway; N: coordination number; R: bond distance;  $\Delta E$ : the inner potential correction. The obtained XAFS data was processed in Athena (version 0.9.25) for background, pre-edge line and post-edge line calibrations. The data range adopted for data fitting in k-space and R space are 3-11.5 Å<sup>-1</sup> and 1-3 Å, respectively.

**Supplementary Table 5. Excitation properties based on the wavefunctions of Melem\_3.**

	Molecule orbital contribution (Hole)			Molecule orbital contribution (Electron)				Molecule orbital contribution (Hole)			Molecule orbital contribution (Electron)		
S0→S1	MO	151	14.071%	MO	154	68.397%		MO	138	16.530%	MO	154	51.954%
	MO	152	27.839%	MO	155	14.459%	S0→S9	MO	143	22.826%	MO	155	17.193%
	MO	153	50.968%	MO	157	6.912%		MO	145	9.484%	MO	156	8.394%
S0→S2	MO	151	28.569%	MO	154	18.080%		MO	137	19.313%	MO	154	29.615%
	MO	152	15.441%	MO	155	62.993%	S0→S10	MO	138	11.299%	MO	155	37.942%
	MO	153	48.866%	MO	157	9.812%		MO	150	11.187%	MO	160	7.391%
S0→S3	MO	151	37.218%	MO	154	37.462%		MO	151	36.625%	MO	154	33.124%
	MO	152	37.269%	MO	155	37.027%	S0→S11	MO	152	15.992%	MO	155	14.635%
	MO	153	17.695%	MO	157	13.292%		MO	153	26.999%	MO	156	27.816%
S0→S4	MO	150	47.527%	MO	154	20.177%		MO	151	3.065%	MO	155	34.473%
	MO	151	8.132%	MO	155	57.173%	S0→S12	MO	152	34.192%	MO	156	33.596%
	MO	152	9.408%	MO	156	11.088%		MO	153	35.353%	MO	162	11.681%
S0→S5	MO	146	16.036%	MO	154	39.300%		MO	151	26.303%	MO	154	23.953%
	MO	149	15.260%	MO	155	32.108%	S0→S13	MO	152	7.807%	MO	155	18.083%
	MO	150	20.259%	MO	156	10.911%		MO	153	40.502%	MO	156	36.970%
S0→S6	MO	146	7.248%	MO	154	44.219%		MO	138	22.850%	MO	154	44.924%
	MO	148	33.220%	MO	155	23.903%	S0→S14	MO	141	33.109%	MO	157	12.639%
	MO	149	13.611%	MO	157	7.874%		MO	142	18.279%	MO	158	29.103%
S0→S7	MO	136	13.136%	MO	154	37.571%		MO	140	22.905%	MO	154	16.970%
	MO	143	6.749%	MO	155	28.780%	S0→S15	MO	142	26.607%	MO	155	33.323%
	MO	150	30.250%	MO	160	7.516%		MO	152	8.676%	MO	157	21.247%
S0→S8	MO	136	13.859%	MO	154	40.885%		MO	140	33.930%	MO	155	33.086%
	MO	137	17.967%	MO	155	29.284%	S0→S16	MO	141	24.611%	MO	157	28.433%
	MO	138	10.097%	MO	160	9.744%		MO	142	6.556%	MO	159	15.597%

**Supplementary Table 6. Excitation properties based on the wavefunctions of Melem\_3Na+.**

	Molecule orbital contribution (Hole)			Molecule orbital contribution (Electron)				Molecule orbital contribution (Hole)			Molecule orbital contribution (Electron)		
S0→S1	MO	156	16.370%	MO	159	50.714%	S0→S9	MO	150	16.143%	MO	159	32.219%
	MO	157	28.906%	MO	160	28.431%		MO	151	14.245%	MO	160	18.088%
	MO	158	47.236%	MO	165	9.882%		MO	152	23.079%	MO	162	16.494%
S0→S2	MO	156	28.665%	MO	159	28.572%	S0→S10	MO	150	17.206%	MO	159	24.905%
	MO	157	16.793%	MO	160	50.573%		MO	151	17.064%	MO	160	22.652%
	MO	158	47.059%	MO	165	9.935%		MO	152	15.489%	MO	165	17.995%
S0→S3	MO	156	38.540%	MO	159	36.710%	S0→S11	MO	151	19.316%	MO	154	33.124%
	MO	157	37.923%	MO	160	37.005%		MO	152	19.447%	MO	155	33.136%
	MO	158	16.787%	MO	165	13.014%		MO	153	8.630%	MO	156	14.383%
S0→S4	MO	147	15.135%	MO	159	37.061%	S0→S12	MO	143	9.834%	MO	159	28.788%
	MO	148	15.314%	MO	160	37.519%		MO	157	18.907%	MO	160	27.355%
	MO	151	8.723%	MO	161	13.147%		MO	158	10.371%	MO	161	18.108%
S0→S5	MO	148	13.833%	MO	159	24.221%	S0→S13	MO	142	9.828%	MO	159	27.347%
	MO	149	20.893%	MO	160	48.620%		MO	156	18.948%	MO	160	28.782%
	MO	152	12.584%	MO	161	10.043%		MO	158	10.349%	MO	161	18.116%
S0→S6	MO	147	14.340%	MO	159	49.006%	S0→S14	MO	141	10.630%	MO	159	28.119%
	MO	149	20.718%	MO	160	23.845%		MO	141	18.961%	MO	160	28.836%
	MO	152	12.348%	MO	161	10.014%		MO	142	16.524%	MO	161	16.263%
S0→S7	MO	145	15.746%	MO	159	28.623%	S0→S15	MO	141	10.658%	MO	159	28.819%
	MO	146	15.655%	MO	160	28.829%		MO	156	18.931%	MO	160	28.102%
	MO	158	15.053%	MO	162	10.142%		MO	158	16.474%	MO	161	16.249%
S0→S8	MO	150	14.208%	MO	159	16.990%							
	MO	151	15.924%	MO	160	33.282%							
	MO	152	23.405%	MO	162	16.511%							

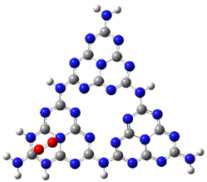
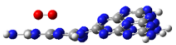
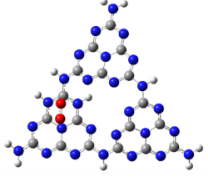
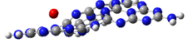

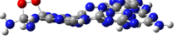
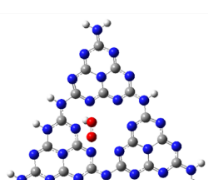
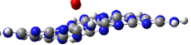


**Supplementary Table 7. Excitation properties based on the wavefunctions of Melem\_3Sb3+.**

Molecule orbital contribution (Hole)				Molecule orbital contribution (Electron)				Molecule orbital contribution (Hole)				Molecule orbital contribution (Electron)			
S0→S1	MO	149	3.633%	MO	155	<b>99.112%</b>		MO	146	37.096%	MO	155	<b>40.942%</b>		
	MO	151	65.610%					S0→S14	MO	153	11.569%	MO	156	27.918%	
	MO	154	19.339%					MO	154	11.569%	MO	157	10.666%		
S0→S2	MO	149	17.637%	MO	155	<b>98.594%</b>		MO	141	11.460%	MO	155	<b>37.232%</b>		
	MO	151	13.214%					S0→S15	MO	151	23.242%	MO	156	20.075%	
	MO	154	50.549%					MO	154	12.858%	MO	157	27.434%		
S0→S3	MO	150	12.440%	MO	155	<b>98.773%</b>		MO	147	10.948%	MO	155	<b>64.773%</b>		
	MO	152	17.901%					S0→S16	MO	148	37.814%	MO	156	6.228%	
	MO	153	54.845%					MO	151	13.782%	MO	157	17.977%		
S0→S4	MO	144	7.421%	MO	155	<b>99.225%</b>		MO	146	20.726%	MO	155	<b>44.139%</b>		
	MO	150	32.476%					S0→S17	MO	151	11.805%	MO	156	27.976%	
	MO	153	36.790%					MO	153	11.062%	MO	157	10.670%		
S0→S5	MO	141	32.952%	MO	155	<b>98.441%</b>		MO	141	18.967%	MO	155	<b>77.536%</b>		
	MO	145	32.842%					S0→S18	MO	142	35.504%	MO	156	5.924%	
	MO	154	22.604%					MO	147	20.012%	MO	157	4.105%		
S0→S6	MO	143	12.371%	MO	155	<b>98.625%</b>		MO	147	10.237%	MO	157	55.007%		
	MO	150	11.062%					S0→S19	MO	148	83.253%	MO	163	5.986%	
	MO	152	61.864%									MO	164	20.416%	
S0→S7	MO	141	9.700%	MO	155	<b>95.897%</b>		MO	139	14.951%	MO	155	<b>49.783%</b>		
	MO	145	31.267%					S0→S20	MO	146	25.432%	MO	156	20.017%	
	MO	149	34.516%					MO	147	23.178%	MO	157	6.417%		
S0→S8	MO	139	7.962%	MO	155	<b>97.100%</b>		MO	146	36.714%	MO	155	<b>21.729%</b>		
	MO	143	23.509%					S0→S21	MO	147	41.974%	MO	156	31.893%	
	MO	144	49.833%					MO	148	4.249%	MO	157	14.042%		
S0→S9	MO	143	37.403%	MO	155	<b>98.014%</b>		MO	139	16.928%	MO	155	<b>64.457%</b>		
	MO	144	28.745%					S0→S22	MO	140	24.402%	MO	156	15.844%	
	MO	150	14.566%					MO	146	21.073%	MO	157	5.920%		
S0→S10	MO	152	9.902%	MO	155	8.267%		MO	145	19.544%	MO	155	<b>29.565%</b>		
	MO	153	22.497%	MO	156	26.006%		S0→S23	MO	151	8.865%	MO	156	28.095%	
	MO	154	42.826%	MO	157	43.742%		MO	152	16.424%	MO	157	11.023%		
S0→S11	MO	145	12.654%	MO	155	<b>86.894%</b>		MO	138	38.207%	MO	155	<b>47.750%</b>		
	MO	148	41.191%	MO	156	4.160%		S0→S24	MO	153	8.226%	MO	156	12.316%	
	MO	149	16.773%	MO	157	2.632%		MO	154	8.707%	MO	157	17.450%		
S0→S12	MO	142	38.982%	MO	155	<b>84.579%</b>		MO	146	21.944%	MO	155	<b>19.032%</b>		
	MO	146	6.215%	MO	156	5.009%		S0→S25	MO	147	24.951%	MO	156	12.536%	
	MO	147	43.746%	MO	162	2.747%		MO	148	15.529%	MO	157	27.791%		
S0→S13	MO	139	20.544%	MO	155	<b>87.222%</b>		MO	137	21.180%	MO	155	<b>22.031%</b>		
	MO	140	27.510%	MO	156	4.259%		S0→S26	MO	146	35.194%	MO	158	20.115%	
	MO	146	19.057%	MO	157	2.552%		MO	147	22.580%	MO	165	14.447%		

It is noteworthy that the absorption edge of simulated UV spectra as well as computed optical gaps are usually larger than the experimental band gaps because of the following two reasons: (1) To simulate the charge-transfer properties of the model with high qualities, function of  $\omega$ B97XD, a function including large amount of Hartree–Fock exchange, was used. These exchange functions usually overestimate the excitation energies, as well as the simulated HOMO-LUMO gap; (2) In the solid state, p-conjugated molecules adjacent to the one carrying a charge strongly polarize, an effect that stabilizes the cationic and anionic states (each generally by about one eV in p-conjugated materials). In this case, the experimental band gap is typically considerably smaller in energy than the calculated molecular fundamental gap, as well as the calculated optical gap<sup>11</sup>. Since the system error cannot be eliminated, the possible simulated ES that contributed to H<sub>2</sub>O<sub>2</sub> production (corresponding to the spectra from 420 nm – 470 nm) were confirmed by comparing the experimental spectra and simulated ones. Then, the transition density of electron/holes was considered at all these ES.

**Supplementary Table 8. Initial and optimized configuration for investigating the side-on adsorption of O<sub>2</sub> on PCN surface.**

	Side-on adsorption of O <sub>2</sub> on Melem_3 (Site 1)		Side-on adsorption of O <sub>2</sub> on Melem_3 (Site 2)	
	Top view	Side view	Top view	Side view
Before optimization				
After optimization				

## Supplementary Notes 1: Probing WOR and ORR with low-concentration electron acceptor

To calculate the  $\text{H}_2\text{O}_2$  generated from the Sb-SAPC system, we made the following assumptions: (1) all added  $\text{Ag}^+$  (4n mol) is consumed to provide holes to generate the initial  $\text{O}_2$  (n mol); (2) then, the Sb-SAPC reduces  $\text{O}_2$  (n mol) to form  $\text{H}_2\text{O}_2$  (n mol) and simultaneously oxidizes  $\text{H}_2\text{O}$  (n mol) to generate fresh  $\text{O}_2$  (1/2n mol); (3) the  $\text{O}_2$  generated in (2) keeps participating in the  $\text{H}_2\text{O}_2$  production and WOR to generate  $\text{O}_2$  (1/4n, 1/8n, 1/16n... mol) until all  $\text{O}_2$  is completely consumed. As a result, the amount of  $\text{H}_2\text{O}_2$  produced by the initially generated  $\text{O}_2$  can be calculated as follows:

$$n_{\text{H}_2\text{O}_2} = \sum_{k=1}^x n_{\text{O}_2} r^{k-1} = \frac{n_{\text{O}_2}(1-r^x)}{1-r} \quad (1)$$

where  $n_{\text{H}_2\text{O}_2}$  is the generated amount of  $\text{H}_2\text{O}_2$ ,  $n_{\text{O}_2}$  is the amount of generated  $\text{O}_2$  by  $\text{Ag}^+$ ,  $r$  is 1/2,  $k$  is number of reaction cycles for simultaneous  $\text{H}_2\text{O}_2$  production and WOR. If the initial  $\text{O}_2$  generated by  $\text{Ag}^+$  ( $k = 1$ ) was all consumed for  $\text{H}_2\text{O}_2$  production (i.e.,  $k$  equals to  $\infty$ ), the total amount of  $\text{H}_2\text{O}_2$  produced would be 2 times the amount of  $\text{O}_2$  ( $k = 1$ ) and 1/2 times the amount of added  $\text{Ag}^+$ . The constant concentration of  $\text{H}_2\text{O}_2$  was measured to be 0.032 mM with addition of 200 mg catalyst, 64% of the ideal value (0.05 mM) calculated based on the initially added  $\text{Ag}^+$  (0.1 mM). The 36% deficiency of  $\text{H}_2\text{O}_2$  could be due to the reaction equilibrium of  $\text{H}_2\text{O}_2$  production<sup>9,12</sup> and the dissolved  $\text{O}_2$  in aqueous solution ( $\text{O}_2$  solubility in pure water: 0.25 mM).

## Supplementary Notes 2: Investigation of synthesis process of Sb-SAPC

The synthesis of Sb-SAPC was first investigated to give a view of the structure of Sb-SAPC. Sb-ethoxide was formed after dissolving  $\text{NaSbF}_6$  in ethanol. After addition of melamine, the lattice distance of the Sb-containing mixture was slightly increased. The formed Sb-containing compound can be assigned to the Sb-melamine, verified by X-ray diffraction (XRD, [Supplementary Figure 13a](#)) and X-ray photoelectron spectroscopy (XPS, [Supplementary Figures 14-15](#)). Then, thermal polymerization and removal of F element were performed by calcination at 560 °C for 4 hours ([Supplementary Figure 16](#)).

The calcination temperature was also investigated. Sb-SAPC5 (5 mmol of  $\text{NaSbF}_6$

mixed with 4 g of melamine were used as the precursor) was prepared at 520 °C and 560 °C (named as Sb-SAPC5\_520 and Sb-SAPC5\_560), respectively. As shown in [Supplementary Figure 17a](#), the inner-panel diffraction of the (100) lattice completely disappears in Sb-SAPC5\_520, and the inter-panel diffraction of PCN (002) lattice is also significantly decreased in Sb-SAPC5\_560, while the crystalline structure of graphitic carbon nitride maintains. Additionally, the F element cannot be completely eliminated by heating at 520 °C, as shown in the XPS measurement ([Supplementary Figure 17b](#)). These results imply that low calcination temperature cannot remove the F element in the PCN matrix, leading to an incomplete polymerization of the graphitic carbon nitride<sup>13</sup>. Additionally, the Sb-SAPC5\_520 shows much poorer photocatalytic activity toward H<sub>2</sub>O<sub>2</sub> production, even worse than the pristine PCN ([Supplementary Figure 17c](#)). Therefore, Sb-SAPCs prepared at 560 °C were used for further photocatalytic investigation.

### **Supplementary Notes 3: Structure characterization**

The crystalline structures of the as-prepared samples were examined by XRD and HRTEM. XRD patterns of all Sb-SAPC samples show two characteristic peaks at about 27.6° and 13.1° ([Supplementary Figure 19](#)), which can be ascribed to the interlayer stacking (002) and the inter planar structure packing (100) of tri-s-triazine units, respectively<sup>14</sup>. The slight shift in the diffraction angle of the (002) peak for Sb-SAPC15 can be attributed to the electrostatic repulsion between interlayers when positive ions are incorporated into the PCN matrix. The intensities of these two peaks gradually decrease when increasing the contents of precursors ([Supplementary Figure 19c](#)), indicating that polymeric structure of melon/g-C<sub>3</sub>N<sub>4</sub> could be slightly influenced by the foreign ions<sup>15</sup>. Although the long-range order of the (002) and (100) lattices significantly decreases, these two lattices can still be observed even when the content of ions reaches as high as 20 mmol. To further investigate whether the pristine structure is changed after the ion incorporation, high-resolution TEM measurements of the exfoliated Sb-SAPC were conducted (as shown in [Supplementary Figure 20](#)). The (100) inter planar structure packing of the tri-s-triazine units can be readily observed, and the lattice distance is

determined to be 6.81 Å, which is in accordance with the XRD results. Thus, the crystalline structure of melon can be well preserved in Sb-SAPC.

#### **Supplementary Notes 4: Influence of the -C≡N group**

FT-IR ([Supplementary Figure 24a](#)) and XPS measurements reveal the existence of -C≡N groups in both PCN\_Na15 and Sb-SAPC15. The interrelationship between -C≡N groups and cations in carbon nitride matrix was investigated. As shown in [Supplementary Figure 24a](#), the absorption band around the wavenumber of 2180 cm<sup>-1</sup> in the spectrum of PCN\_Na15 is slightly stronger than that in the spectrum of Sb-SAPC15, manifesting the larger content of -C≡N groups in PCN\_Na15. To investigate the influence of the cation content on the formation of -C≡N groups, ICP measurements were performed. As shown in [Supplementary Table 2](#), the Na amount in PCN\_Na15 (0.87 mmol per gram) and Sb-SAPC15 (0.66 mmol per gram) are close, while PCN\_Na15 contains no Sb species. Additionally, the ratios of the integration areas from the deconvoluted peaks at 288.1 and 286.5 eV are similar in the high-resolution XPS spectra of PCN\_Na15 (0.268) and Sb-SAPC15 (0.228). These results indicate that the introduction of Sb sites into PCN has little influence on the formation of -C≡N groups, and the -C≡N group formation could be possibly due to the incorporation of alkaline metal ions<sup>10</sup>. These results are also in accordance with the proposed synthesis mechanism ([Supplementary Figure 1](#)) and the EXAFS fitting results.

Several studies have reported that the -C≡N is an electron-withdrawing group that may significantly enhance the charge separation, and thus improve the photocatalytic activity<sup>10, 15-17</sup>. To clarify the influence of -C≡N groups and Sb species on charge separation and photocatalytic activity, a comprehensive investigation has to be carried out by comparing the photocatalytic performance of Sb-SAPC15 and PCN\_Na15. As clarified in the previous paragraph, the Na ion content in Sb-SAPC15 is similar to that in PCN\_Na15, giving a similar -C≡N content. But Sb-SAPC15 exhibits a much higher photocatalytic activity ([Figure 1c](#) and [Supplementary Figure 9b](#)), suggesting the crucial function of the Sb species for photocatalysis. Additionally, the photoluminescence intensity of PCN\_Na15

([Supplementary Figure 31a](#)) is weaker as compared to that of pristine PCN, indicating that the charge recombination can be effectively suppressed by introducing the  $-C\equiv N$  groups. In the case of Sb-SAPC15, the introduction of Sb species can further decrease the photoluminescence intensity, manifesting that the radiative recombination is suppressed. The TRPL spectrum also shows the similar phenomenon, i.e. lifetime of the charge carriers in Sb-SAPC15 (0.428 ns) is shorter than that in PCN\_Na15 (1.41 ns), indicating that non-radiative recombination is facilitated in Sb-SAPC15.

### **Supplementary Notes 5: Post characterization and investigation for catalyst poisoning**

The HAADF STEM image of Sb-SAPC15 after 5 days of photoreaction shows that the Sb sites remain atomically dispersed ([Supplementary Figure 29a](#)). The UV-vis spectra show that the light absorption property of Sb-SAPC15 was hardly influenced by the continuous photoreaction ([Supplementary Figure 29b](#)). The XRD pattern indicates that the crystallinity of Sb-SAPC15 hardly changed after 5 days of photoreaction. Note that both diffractions at  $13.1^\circ$  and  $27.4^\circ$  are clearly observable, indicating that the PCN structure in Sb-SAPC15 was well maintained after long-term photoreaction ([Supplementary Figure 29c](#)). High-resolution N 1s, C 1s, O 1s and Sb 3d XPS spectra show that the chemical states of N, C, O and Sb on the surface of Sb-SAPC15 were hardly influenced by the long-time photoreaction ([Supplementary Figure 29d-f](#)). The surface oxidation of CN and Sb were not observed. All of the above results demonstrate the excellent photocatalytic stability of Sb-SAPC15.

The maximum  $H_2O_2$  concentration after 8 h of photocatalytic reaction is approximately 0.016 wt.% of  $H_2O_2$ . Thus to further investigate whether catalyst poisoning occurred on the surface of the catalyst, the photocatalytic activity was measured after soaking the as-prepared Sb-SAPC15 catalyst in different concentrations of  $H_2O_2$  solution (ranging from 0.01 wt.% to 1 wt.%) for 8 h. The photocatalytic activity of Sb-SAPC15 showed no obvious decay after being soaked in different concentrations of  $H_2O_2$  solution for 8 h. This result indicates insignificant catalyst poisoning during our photocatalytic  $H_2O_2$  production process.

## Supplementary Notes 6: Optical properties and action spectra

As shown in the insert to [Supplementary Figure 30a](#), Sb-SAPC15 displays a deep yellow color, darker than the pale yellow color of pristine PCN and PCN\_Na15. To determine the precise band positions of these samples, UV-vis spectroscopy, Mott-Schottky and valence band XPS measurements were conducted to obtain the bandgap width, CBM and VBM, respectively. As shown in [Supplementary Figure 30a-b](#), the light absorption ( $\lambda < 450$  nm) of Sb-SAPC15 significantly enhances compared with that of PCN\_Na15 and pristine PCN, possibly due to changes in electronic states resulted from Sb incorporation. Tauc plots of pristine PCN, PCN\_Na15 and Sb-SAPC15 indicate that the bandgap almost keeps constant after introducing Sb and/or Na ions. VB-XPS results show that the VBM of PCN\_Na15 and Sb-SAPC15 keep almost the same ( $\sim 1.45$  eV) to that of PCN ([Supplementary Figure 30c](#)). Mott-Schottky plots reveal that the CBM slightly become more positive from pristine PCN to PCN\_Na15 and to Sb-SAPC15 ([Supplementary Figure 30d-f](#)). By summarizing these results for band positions, we draw the band position diagrams of these samples, as shown in [Supplementary Figure 30g](#).

The action spectra of Sb-SAPC15 ([Figure 1c](#)) show that the apparent quantum yield ( $\Phi_{AQY}$ ) agrees well with the absorption spectrum ([Supplementary Figure 30a](#)). The absorption in the wavelength larger than 500 nm of Sb-SAPC15 could not contribute to the production of  $H_2O_2$ . These results show that the VB-to-CB excitation of Sb-SAPC15 is responsible for the  $H_2O_2$  production.

## Supplementary Notes 7: Verification of WOR mechanism

OER occurred in our photocatalytic system for the following reasons:

- 1) We have checked the water oxidation reaction by adding the electron acceptor of  $NaIO_3$  to make sure whether molecular oxygen could indeed be produced. As shown in [Figure 1f](#), oxygen was gradually generated in the system of Sb-SAPC15, while neither  $O_2$  nor  $H_2O_2$  could be detected in the system of pristine PCN and PCN\_Na15.
- 2) We have observed that the deeply trapped electrons (at  $5000\text{ cm}^{-1}$ ) in Sb-SAPC15



were significantly decelerated by TR-IR after addition of 20 Torr water (Figure 3b). This result indicates that the photogenerated holes were consumed by water oxidation reaction so that the lifetime of photogenerated electrons was significantly prolonged. In the case of PCN and PCN\_Na15, the lifetime of photogenerated electrons kept almost the same (PCN\_Na15) or even decreased after addition of water into the system, indicating that the photogenerated holes could barely participate in the water oxidation reaction. These results confirm that the activity of water oxidation for Sb-SAPC is significantly higher than that for PCN or PCN\_Na15.

3) To further investigate the oxygen evolution reaction (OER), rotating ring-disk electrode measurement was conducted. The anodic polarization curves of the rotating ring-disk electrode modified by PCN, PCN\_Na15 and Sb-SAPC15 were recorded. As shown in Supplementary Figure 34a, the disk current of the electrode modified by Sb-SAPC15 is significantly larger than that of the electrode modified by PCN or PCN\_Na15, indicating that the rate of the oxidation reaction taking place on the surface of Sb-SAPC15 is faster than that on PCN and PCN\_Na15 (Supplementary Figure 34b). More importantly, clear signals of O<sub>2</sub> reduction to H<sub>2</sub>O were detected by the ring electrode in both cases of Sb-SAPC15 with or without light irradiation, verifying O<sub>2</sub> generation on the Sb-SAPC15 surface via WOR (Supplementary Figure 34c). Moreover, the ring current of the electrode modified by Sb-SAPC15 under light irradiation is obviously larger than that in the dark condition, indicating that photo-induced holes indeed facilitated the WOR. Furthermore, the anodic current on the ring electrode under light irradiation appeared much earlier than that in the dark condition, which also manifested that the photogenerated holes participated in the OER (Supplementary Figure 34d). Therefore, the highly active photo-generated holes boosted the OER via the WOR pathway in the Sb-SAPC15 system.

The water oxidation reaction took place on N atoms of carbon nitride, rather than on the Sb atoms, because of the following reasons:

1) Photocatalytic reaction occurs on the surface of a photocatalyst. The excitation properties on the surface of photocatalysts have been widely investigated by the cluster models, such as N-doped TiO<sub>2</sub><sup>18</sup> and In<sub>2</sub>O<sub>3</sub><sup>19</sup>. The excitation can be systematically

discussed by combining the simulated UV-vis spectra and transition densities of charge carriers. As shown in [Supplementary Figure 37a-c](#), the shape of the computed UV-vis absorption spectrum is almost the same as that obtained experimentally, especially in the wavelength between 420 nm and 470 nm. To give a comprehensive understanding of the transition densities of electrons/holes for boosting the  $\text{H}_2\text{O}_2$  production, all transition densities of the 50 excited states (ES) were summarized in [Supplementary Figure 37d-i](#). Electrons are mostly distributed at the C atoms and Sb atoms, while holes are mostly distributed at the N sites. To further investigate the excitations that contribute to photocatalytic  $\text{H}_2\text{O}_2$  production, the excited states 1-16 of Melem\_3, ES 1-15 of Melem\_3Na<sup>+</sup> and ES 1-26 of Melem\_3Sb<sup>3+</sup> were highlighted in these figures. On the one hand, most of electrons are accumulated at the Sb sites (ES 1-26) of Melem\_3Sb<sup>3+</sup> with high density (~20-80%), while most of states show averagely distributed electrons at the C sites (< mostly 20%) in the cluster model of Melem\_3 and Melem\_3Na<sup>+</sup>. On the other hand, holes are distributed at the N atoms on Melem\_3Sb<sup>3+</sup>, Melem\_3 and Melem\_3Na<sup>+</sup>.

The boundary effect of small cluster models in [Supplementary Figure 37](#) confined the distance of possible separated charges. To give a comprehensive assessment of charge separation by TDDFT simulation, we built larger models to represent pristine PCN (Melem\_6), sodium incorporated PCN (Melem\_6Na<sup>+</sup>) and single atomic Sb incorporated PCN (Melem\_6Sb<sup>3+</sup>) to simulate the properties of charge separation ([Supplementary Figure 38](#)). Based on the action spectra and the photocatalytic  $\text{H}_2\text{O}_2$  production activities, the ES 1-26 of Melem\_6, the ES 1-26 of Melem\_6Na<sup>+</sup> and the ES 3-30 of Melem\_6Sb<sup>3+</sup> are highlighted in the distribution heatmap of photogenerated electrons and holes ([Supplementary Figure 39d-i](#)). It is confirmed that most of the electrons are accumulated at the Sb sites (ES 3-30, Melem\_6Sb<sup>3+</sup>), a ligand-to-metal charge transfer from neighboring melem units to Sb, while most of the states (ES 1-26 for Melem\_6 and Melem\_6Na<sup>+</sup>) show averagely distributed electrons at the C sites. The photogenerated electrons and holes barely locate at the Na atoms, indicating that the coordinated Na species on the catalyst's surface unlikely serve as the active sites for the photocatalytic reaction. The above results from Melem\_6, Melem\_6Na<sup>+</sup> and Melem\_6Sb<sup>3+</sup> give almost the same electronic

configurations as the results from Melem\_3, Melem\_3Na<sup>+</sup> and Melem\_3Sb3<sup>+</sup> (Supplementary Figure 37d-i).

To investigate the properties of charge separation in these three models, the most important transitions that can participate in the photocatalytic H<sub>2</sub>O<sub>2</sub> production were figured out by checking the oscillator strength of each transition in the UV spectra (as shown in the orange dash circles; i. e., the transitions of ES25 and ES26 of Melem\_6, ES9~ES26 of Melem\_6Na<sup>+</sup> and ES3~ES30 of Melem\_6Sb3<sup>+</sup>)<sup>19</sup>. We then calculated the distance between centroid of hole and electron (D index) in these transitions. This D index was defined followed by the Manual of the Multiwfn<sup>20,21</sup>, which could reveal whether charge separation of photogenerated electron hole pair is efficient. As shown in Supplementary Figure 40a, all of the D index of the transitions of Melem\_6Sb3<sup>+</sup> (ES3~ES30) are significantly larger than that of Melem\_6 (ES25 and ES26) and Melem\_6Na<sup>+</sup> (ES9~ES26), indicating that the charge separation is significantly boosted after the introduction of atomic antimony sites.

Additionally, another crucial property of photogenerated positive charge carriers (photogenerated holes or positive polarons) for facilitating WOR is their high localization levels. To simulate the localization level of photogenerated electrons and holes, we calculated the hole delocalization index (HDI) and electron delocalization index (EDI)<sup>20,21</sup> as defined below:

$$HDI = 100 \times \sqrt{\int [\rho^{hole}(r)]^2 dr} \quad (2)$$

$$EDI = 100 \times \sqrt{\int [\rho^{ele}(r)]^2 dr} \quad (3)$$

$\rho^{hole}$  and  $\rho^{ele}$  respectively indicate the distribution density of holes and electrons<sup>20,21</sup>.

It is found that the smaller the HDI (EDI) is, the larger the spatial delocalization of holes (electrons). HDI and EDI are useful in quantifying breadth of spatial distribution for electrons and holes. As shown in Supplementary Figure 40b-c, the HDI and EDI of the transitions of Melem\_6Sb3<sup>+</sup> (ES3~ES30) are significantly larger than those of Melem\_6 (ES25 and ES26) and Melem\_6Na<sup>+</sup> (ES9~ES26), indicating that both of the electrons and holes are highly concentrated after introduction of single atomic antimony sites.

2) Additionally, the computational hydrogen electrode (CHE) method also confirmed the preferred 2e<sup>-</sup> ORR pathway on Sb-SAPC (Supplementary Figure 42). This free energy

diagram could also be used to study the OER activity of Sb sites since the backward reaction for  $4e^-$  ORR is  $4e^-$  OER. It can be seen that the difference between  $^*OH$  and  $^*O$  is as high as 3.742 eV, indicating that a considerably large energetic barrier needs to be overcome for the  $4e^-$  OER process. In this case, the Sb site should not function as an effective site to catalyze  $4e^-$  OER.

Based on the above evidence, we can draw a conclusion that the Sb sites work as the  $2e^-$  ORR sites, and the N atoms on melem units work as the  $4e^-$  OER sites.

### **Supplementary Notes 8: Simulated Raman spectra for verification of adsorption configurations of $O_2$**

To investigate the side-on adsorption of  $O_2$  on PCN, we have re-calculated the possible adsorption configurations of  $O_2$  on PCN. In our case, a function of  $\omega97xd$  at 6-311g(d) level was used for optimization to investigate the most favorable adsorption site for  $O_2$  on PCN. The initial and optimized configurations are summarized in [Supplementary Table S8](#). The calculation results show that the distance between  $O_2$  and Melem\_3 gradually increased during the optimization process. Therefore, the side-on adsorption of  $O_2$  is not possible on site 2. On the contrary,  $O_2$  can be adsorbed on site 1 of PCN with similar configuration to the previous literature. The distance between  $O_2$  and the Melem unit is less than 1.5 Å. This bond length indicates that  $O_2$  can be chemically adsorbed on site 1 with a typical side-on adsorption configuration.

To further understand the influence of  $O_2$  adsorption configuration on the Raman spectrum, we calculated the Raman spectra of the optimized structure for Melem\_3 and Melem\_3Sb3+ after  $O_2$  adsorption. The Raman spectra of Melem\_3 and Melem\_3Sb3+ before  $O_2$  adsorption were also calculated for comparison ([Supplementary Figure 44](#)). A new chemical shift appears at around  $820\text{ cm}^{-1}$  ([Supplementary Figure 44b](#)) after  $O_2$  adsorption on Melem\_3. Similarly, a new chemical shift appears at around  $780\text{ cm}^{-1}$  ([Supplementary Figure 44d](#)) after  $O_2$  adsorption on the Sb sites in Melem\_3Sb3+. The relative position tendency of the changes in these newly observed chemical shifts are similar to the experimental results.

## Supplementary References

- [1] Shiraishi, Y. *et al.* Resorcinol–formaldehyde resins as metal-free semiconductor photocatalysts for solar-to-hydrogen peroxide energy conversion, *Nat. Mater.* **18**, 985-993 (2019).
- [2] Gao, J. *et al.* Enabling direct H<sub>2</sub>O<sub>2</sub> production in acidic media through rational design of transition metal single atom catalyst, *Chem* **6**, 1-17 (2020).
- [3] Shiraishi, Y. *et al.* Sunlight-driven hydrogen peroxide production from water and molecular oxygen by metal-free photocatalysts, *Angew. Chem.* **126**, 13672-13677 (2014).
- [4] Kofuji, Y. *et al.* Carbon nitride–aromatic diimide–graphene nanohybrids: Metal-free photocatalysts for solar-to-hydrogen peroxide energy conversion with 0.2% efficiency, *J. Am. Chem. Soc.* **138**, 10019-10025 (2016).
- [5] Kofuji, Y. *et al.* Hydrogen peroxide production on a carbon nitride-boron nitride-reduced graphene oxide hybrid photocatalyst under visible light, *ChemCatChem* **10**, 2070-2077 (2018).
- [6] Kaynan, N., Berke, B.A., Hazut, O. & Yerushalmi, R. Sustainable photocatalytic production of hydrogen peroxide from water and molecular oxygen, *J. Mater. Chem. A* **2**, 13822–13826 (2014).
- [7] Wang, L. *et al.* Simultaneous hydrogen and peroxide production by photocatalytic water splitting, *Chin. J. Catal.* **40**, 470-475 (2019).
- [8] Hou, W.-C. & Wang, Y.-S. Photocatalytic generation of H<sub>2</sub>O<sub>2</sub> by graphene oxide in organic electron donor-free condition under sunlight, *ACS Sustainable Chem. Eng.* **5**, 2994–3001 (2017).
- [9] Kofuji, Y. *et al.* Mellitic triimide-doped carbon nitride as sunlight-driven photocatalysts for hydrogen peroxide production, *ACS Sustainable Chem. Eng.* **5**, 6478-6485 (2017).
- [10] Qiu, C. *et al.* Photocatalysis: highly crystalline K-intercalated polymeric carbon nitride for visible-light photocatalytic alkenes and alkynes deuterations, *Adv. Sci.* **6**, 1970002 (2019).
- [11] Bredas, J.-L. Mind the gap! *Mater. Horiz.* **1**, 17-19 (2014).
- [12] Qu, X. *et al.* The effect of embedding N vacancies into g-C<sub>3</sub>N<sub>4</sub> on the photocatalytic H<sub>2</sub>O<sub>2</sub> production ability via H<sub>2</sub> plasma treatment, *Diamond Relat. Mater. J.* **86**, 159-166 (2018).
- [13] Zhu, B., Xia, P., Ho, W. & Yu, J. Isoelectric point and adsorption activity of porous g-C<sub>3</sub>N<sub>4</sub>, *Appl. Surf. Sci.* **344**, 188-195 (2015).
- [14] Teng, Z. *et al.* Bandgap engineering of ultrathin graphene-like carbon nitride nanosheets with controllable oxygenous functionalization, *Carbon* **113**, 63-75 (2017).
- [15] Zhang, P. *et al.* Modified carbon nitride nanozyme as bifunctional glucose oxidase-peroxidase for metal-free bioinspired cascade photocatalysis, *Nat. Comm.* **10**, 940 (2019).
- [16] Kim, S. *et al.* Selective charge transfer to dioxygen on KPF<sub>6</sub>-modified carbon nitride for photocatalytic synthesis of H<sub>2</sub>O<sub>2</sub> under visible light, *J Catal.* **357**, 51-58 (2018).
- [17] Moon, G.-H. *et al.* Eco-friendly photochemical production of H<sub>2</sub>O<sub>2</sub> through O<sub>2</sub> reduction over carbon nitride frameworks incorporated with multiple heteroelements, *ACS Catal.* **7**, 2886-2895 (2017).
- [18] Govind, N., Lopata, K., Rousseau, R., Andersen, A. & Kowalski, K. Visible light absorption of N-doped TiO<sub>2</sub> rutile using (LR/RT)-TDDFT and active space EOMCCSD calculations. *J. Phys. Chem. Lett.* **2**, 2696-2701 (2011).
- [19] Ghuman, K.K. *et al.* Photoexcited surface frustrated Lewis pairs for heterogeneous photocatalytic CO<sub>2</sub> reduction, *J. Am. Chem. Soc.* **138**, 1206-1214 (2016).
- [20] Lu, T. Multiwfn -A Multifunctional Wavefunction Analyzer-Software Manual.

[http://sobereva.com/multiwfn/misc/Multiwfn\\_3.7.pdf](http://sobereva.com/multiwfn/misc/Multiwfn_3.7.pdf) (2020).

- [21] Liu, Z., Lu, T. & Chen, Q. An sp-hybridized all-carboatomic ring, cyclo[18]carbon: Electronic structure, electronic spectrum, and optical nonlinearity, *Carbon* **165**, 461-467 (2020).